

3-22-2012

# Investigation of BCF-12 Plastic Scintillating Coherent Fiber Bundle Timing Properties

Joel S. Gearhart

Follow this and additional works at: <https://scholar.afit.edu/etd>

---

## Recommended Citation

Gearhart, Joel S., "Investigation of BCF-12 Plastic Scintillating Coherent Fiber Bundle Timing Properties" (2012). *Theses and Dissertations*. 1175.  
<https://scholar.afit.edu/etd/1175>

This Thesis is brought to you for free and open access by the Student Graduate Works at AFIT Scholar. It has been accepted for inclusion in Theses and Dissertations by an authorized administrator of AFIT Scholar. For more information, please contact [richard.mansfield@afit.edu](mailto:richard.mansfield@afit.edu).



**INVESTIGATION OF BCF-12 PLASTIC SCINTILLATING COHERENT  
FIBER BUNDLE TIMING PROPERTIES**

THESIS

Joel S. Gearhart, Captain, USAF  
AFIT/NUCL/ENP/12-M02

**DEPARTMENT OF THE AIR FORCE  
AIR UNIVERSITY**

**AIR FORCE INSTITUTE OF TECHNOLOGY**

**Wright-Patterson Air Force Base, Ohio**

DISTRIBUTION STATEMENT A

APPROVED FOR PUBLIC RELEASE; DISTRIBUTION UNLIMITED.

The views expressed in this document are those of the author and do not reflect the official policy or position of the United States Air Force, the United States Department of Defense or the United States Government. This material is declared a work of the U.S. Government and is not subject to copyright protection in the United States.

AFIT/NUCL/ENP/12-M02

INVESTIGATION OF BCF-12 PLASTIC SCINTILLATING COHERENT FIBER  
BUNDLE TIMING PROPERTIES

THESIS

Presented to the Faculty  
Department of Engineering Physics  
Graduate School of Engineering and Management  
Air Force Institute of Technology  
Air University  
Air Education and Training Command  
in Partial Fulfillment of the Requirements for the  
Degree of Master of Science in Nuclear Engineering

Joel S. Gearhart, BS  
Captain, USAF

March 2012

DISTRIBUTION STATEMENT A  
APPROVED FOR PUBLIC RELEASE; DISTRIBUTION UNLIMITED.

AFIT/NUCL/ENP/12-M02

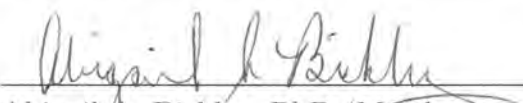
INVESTIGATION OF BCF-12 PLASTIC SCINTILLATING COHERENT FIBER  
BUNDLE TIMING PROPERTIES

Joel S. Gearhart, BS  
Captain, USAF

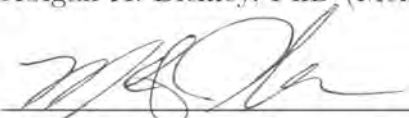
Approved:

  
\_\_\_\_\_  
Maj Benjamin R. Kowash (Chairman)

19 Mar 2012  
Date

  
\_\_\_\_\_  
Abigail A. Bickley, PhD (Member)

3/19/2012  
Date

  
\_\_\_\_\_  
Lt Col Michael R. Hawks (Member)

19 MARCH 2012  
Date

## Abstract

The timing properties of BCF-12 scintillating plastic fibers arranged in a coherent bundle are investigated. An MCNP transport model is developed analyzing the interaction of neutrons with fiber bundles of varying size. A gradient in energy deposition is seen starting at the 10x10 fiber bundles onward. A 40x40 bundle has  $6.7 \pm 0.2\%$  intrinsic efficiency for double scatter events. Over 40% of the double scatter events occur with a time separation of 1 ns or greater in the 40x40 bundle. The lowest dark count rate was achieved with the lens cap / aluminum can and collar system with a dark count rate of 15 per second. A bimodal distribution of scintillation pulse decay constants is discovered; these two distributions are statistically different from each other allowing real-time discrimination of dark events from scintillation events using a single PMT. A dual-ended readout technique is used to investigate scintillation pulse shapes. No significant difference is measured between the multiple peaks seen in scintillation pulses of single fibers and fiber bundles. Multiple scatter events were not detected using a 7x3 fiber bundle. Construction of a 40x40 fiber bundle is recommended for future research due to its intrinsic efficiency and measurable double-scatter event probability.

## Acknowledgements

I'd like to thank my family for their support during my time at AFIT.

Joel S. Gearhart

# Table of Contents

	Page
Abstract .....	iv
Acknowledgements .....	v
List of Figures .....	viii
List of Tables .....	xvi
List of Abbreviations .....	xvii
I. Introduction .....	1
1.1 Background .....	1
1.2 Objectives .....	2
1.3 Thesis Outline .....	2
II. Theory .....	3
2.1 Overview of Scintillators .....	3
2.2 Scintillation Mechanisms in Organics .....	5
2.3 Light Output of Organic Scintillators .....	6
2.4 Time Response of Organic Scintillators .....	7
2.5 BCF-12 Fiber Scintillators .....	8
2.6 Neutron Kinematics with Organic Scintillators .....	11
2.7 Photomultiplier Tubes .....	15
2.8 Digital Data Acquisition .....	17
III. Methodology .....	23
3.1 Simulation of Neutron Radiation on Fiber Bundles .....	23
3.2 Characterizing PMT Dark Counts and Light Leakage .....	25
3.3 Construction of Fiber Bundle .....	29
3.4 Dual-Ended Readout of Fibers .....	34
3.5 Exploration of CCD Capabilities .....	39
IV. Analysis of Results .....	42
4.1 Simulation of Neutron Radiation on Fiber Bundles .....	42
4.2 Characterizing PMT Dark Counts and Light Leakage .....	46
4.3 Dual-Ended Readout of Fibers .....	50
V. Conclusions .....	57
5.1 Conclusions .....	57



	Page
Appendix A. MCNP Particle Track Results . . . . .	59
Appendix B. Representative Fiber Scintillation Pulses . . . . .	62
Appendix C. Scintillation Peak Distributions . . . . .	64
Appendix D. Dual Ended Readout Oscilloscope . . . . .	67
Appendix E. Particle Track Code . . . . .	71
Appendix F. MCNP Input File Generation Code . . . . .	74
Appendix G. Find Maxima Code . . . . .	77
Bibliography . . . . .	80

## List of Figures

Figure		Page
1	Jablonski diagram of an organic molecule with $\pi$ -electron structure [3]. . . . .	4
2.	Energy distribution of recoil protons $E_p$ produced by monoenergetic neutrons. For scattering from hydrogen, $E_p$ is equivalent to $E_R$ [9]. . . . .	7
3.	Diagram of typical Saint-Gobain scintillating fiber [18]. . . . .	10
4.	Neutron kinematics [9]. . . . .	13
5.	Plots of anode pulse for the two extremes of large and small anode time constant [9]. . . . .	16
6.	Top: Individual electrons leaving photocathode. Middle: Current at anode after transit through multiplying structure. Bottom: Leading edge of voltage pulse across anode circuit with long time constant. [9]. . . . .	17
7.	Diagram of dual-ended PMT readout using digital data acquisition. The light output from the scintillator is converted to voltage pulses by the PMTs, which are then measured by the digital oscilloscope. The oscilloscope captures a set number of waveforms digitally to its buffer followed by transferring the buffer to the computer via a gigabit Ethernet connection. . . . .	18
8.	Different arrangement of source and fiber bundle in the MCNP simulations. Parts A, B, and C show the source increasing in distance (5, 10, and 20 cm) from the fiber bundle while staying centered longitudinally and vertically with the bundle. Parts D, E, and F show the source increasing in distance (5, 10, and 20 cm) from the top-left corner of the fiber bundle while staying centered longitudinally with the bundle. Parts G and H are identical to Part A, except the source is located at the far end and close end of the fiber bundle respectively. . . . .	23

9. Aluminum can and collar system. The collar attaches to the PMT tube via set screws. The aluminum can bolts to the collar. The can holds either the NaI crystal or the BC-404 bulk plastic scintillator. For the dark count experiment, the can was empty, no scintillating material was present. The can was used to cut down light leakage onto the PMT. Tape is wrapped around the seam between the collar and can. More tape is wrapped around the gap between the collar and the PMT tube. . . . . 26
10. Image of the large dark box used for three experiments during this investigation. It is designed to be water tight. Water tight doesn't mean light tight, as discovered over the course of this research. . . . . 27
11. Left: Interior BNC connections for two pairs of PMTs. Right: Exterior BNC connections for the PMTs inside the dark box. These connections allowed for the PMT bias and signal cables to be connected while keeping the box completely closed and sealed. . . . . 27
12. A picture of the bulk scintillator used during this investigation. The NaI scintillator is on the left and the BC-404 plastic scintillator is on the right. Electrical tape is wrapped around the plastic scintillator to prevent stray light from radially entering the scintillator medium. The end of the plastic scintillator not facing the PMT window is also blacked out for the same reason. . . . . 28
13. Image of first attempt at constructing a fiber bundle. The 25x25 bundle is framed by standard electronics perfboard. The fibers are cemented to the perfboard by a steel-impregnated binary epoxy. There is an 2.54 mm air gap between each fiber. Bending of the fibers is a noticeable drawback of this method of fiber bundle construction. . . . . 29

Figure	Page
14.	Image of how the fiber ribbons were made. Fibers are held taut and clamped down at both ends. They are anchored to the four supports by double-sided tape. One-minute epoxy (shown at the top-middle of the image) is carefully applied to the fiber ribbon near the clamp ends and in the regions between the supports. . . . . 30
15.	Hot knife used to cleave ends of the fibers used during this investigation. The blade is adapted to attach to the end of a standard electronics soldering iron. . . . . 31
16.	Face view of the fiber bundle taken with CCD camera with magnifying optics. Notice the close packing of the fibers in each row compared to the epoxy bulges separating the three layers. Also note how the top layer isn't lined up with the bottom two layers. . . . . 32
17.	Image of the fully constructed 7x3, no air-gap fiber bundle. The bundle is 19 cm long. A close-up of the bundle face can be found in Figure 16. . . . . 32
18.	Fiber scraps from left from botched attempts at cleaving individual fibers, fiber ribbons, and fiber bundles. The fibers that were used for the fiber ribbon construction started out at 30 cm. When constructed the fiber ribbons ended up at 25 cm. The final bundle measured in at 19 cm. The difficulty in getting a clean fiber cleave resulted in wasting 33% of the initial fiber length. . . . . 33
19.	Illustration of fiber slipping along the PMT window. If the fibers and PMTs are not anchored securely, then fiber slipping can occur. Fiber slipping is problematic for two reasons: the fiber face moves away from the center (most sensitive part) of the PMT window and light from the fiber face has a chance to skip across the PMT window without reaching the photocathode. . . . . 35

20. Image of the cardboard dark box. Electrical tape is triple-wrapped around all faces and edges of the box. Two holes are cut on opposite ends of the box to allow for insertion of the PMTs. A hatch is cut on the top of the box to allow for fiber bundle and radioactive source placement. The advantage of this design is it's darker than the larger plastic dark box used previously, while also being portable. The disadvantage of this design is the fragile nature of the tape adhesive. Changes in temperature made the tape peel off and loosen the PMTs from the box, resulting in fiber slipping. .... 36
21. Full view of the aluminum dark box used for data collection during the dual-ended readout portion of this investigation. The PMTs are secured to the box with set screw after pinching the fiber bundle inside the box. The box is designed with portability in mind, being placed in front of radiation sources that are not found in the laboratory. .... 37
22. Close-up view of the PMT side of the aluminum dark box. Note the electrical tape wrapped around all seams of the box. Also worth noting is the blue putty wrapped around the PMT tube near the aluminum collar. The putty is squeezed between the gap formed by the aluminum collar and PMT tube. It was used because it is easy to pick up and move whenever the PMTs needed to be moved. .... 38
23. Experimental setup of NaI crystal imaging with the CCD camera inside the large dark box. The NaI crystal is placed at the focal length of the camera optics. Half of the crystal is covered with tape. The camera's FOV captures both the mask and the exposed crystal face. A Cs-137 source is placed on top of the crystal. Any scintillation light captured by the camera will only show up on the right side of image. .... 40
24. Experimental setup of 7x3 fiber bundle imaging with the CCD camera inside the large dark box. The closest fiber bundle face to the camera is located at the focal length of the camera optics. A Cs-137 source is placed on top of the bundle, centered along the length of the fibers. .... 41

25.	Progression of energy deposition spectra for 1x1, 2x2, 3x3, 4x4, 5x5, 6x6, 7x7, 8x8, 9x9, 10x10, 15x15, 20x20, 40x40, and 100x100 fiber bundles (left to right, top to bottom). The incident neutron energy is 2.5 MeV. Note the full energy peak that begins to appear at 2.5 MeV from the 15x15 bundle onward. Also worth noting is the peak occurring at around 0.70 MeV corresponding to collisions with carbon in the plastic scintillator. These features are common to all of the plots and become more apparent with larger bundle size. ....	43
26.	MCNP simulated energy deposited per fiber in a 1x1, 2x2, 3x3, 4x4, 5x5, 6x6, 7x7, 8x8, 9x9, 10x10, 15x15, 20x20, 40x40, and 100x100 fiber bundle (left to right, top to bottom). Lighter colors represent more energy deposited than darker colors. The location of the isotropic neutron source is defined by Part A of Figure 8. A noticeable gradient in energy deposition can be seen starting from the 15x15 bundle onward. ....	44
27.	Intrinsic scattering efficiencies for single, double, and triple scatter events as a function of bundle size. ....	45
28.	Distribution of scatter distances for double-scatter events in the 40x40 fiber bundle. ....	46
29.	Distribution of transit energies for double-scatter events in the 40x40 fiber bundle. ....	47
30.	Distribution of scatter times for double-scatter events in the 40x40 fiber bundle. Over 40% of the double scatter events occur with a time separation of 1 ns or greater. ....	47
31.	An example of a dark count waveform captured via a PMT made light-tight with the aluminum can and collar system seen in Figure 9. ....	49
32.	An example of a bulk plastic scintillation event waveform captured via a PMT made light-tight with the aluminum can and collar system seen in Figure 9. ....	49

Figure	Page
33. Comparison of the distribution of decay constants for PMT dark counts and bulk plastic scintillation events. The distributions are separated from each other by 3 standard deviations. Discrimination of noise events from scintillation events can be done at acquisition time using these distributions. ....	50
34. Linear regression analysis used to gain match the two PMTs used during this investigation. From this data it was determined that PMT A would be set to a bias of 2.70 kV, while PMT would be set to a bias of 2.74 kV. These bias settings ensured the response of either PMT would be the same for an identical scintillation light pulse. ....	51
35. Mean voltage distribution for an Am-241 source placed at the center of a single fiber. The distribution is actually comprised to two separate distributions. The peak at the far left shows contribution from noise events such as dark current pulses or light leakage events. The broader distribution to the right of that peak represents actual scintillation events. ....	52
36. Representative waveform measured from the single fiber irradiated with Sr-90. ....	54
37. Representative waveform measured from the 7x3 fiber bundle irradiated with Sr-90. ....	55
38. Distributions of peak separation times measured during Sr-90 irradiation of single fiber and 7x3 fiber bundle. ....	55
39. Distributions of number of peaks measured during Sr-90 irradiation of single fiber and 7x3 fiber bundle. ....	56

40.	MCNP simulated energy deposited per fiber in a 1x1, 2x2, 3x3, 4x4, 5x5, 6x6, 7x7, 8x8, 9x9, 10x10, 15x15, 20x20, 40x40, and 100x100 fiber bundle (left to right, top to bottom). Lighter colors represent more energy deposited than darker colors. Note that the energy scale is identical to that of Figure 26. The location of the isotropic neutron source is defined by Part D of Figure 8. A noticeable gradient in energy deposition can be seen starting from the 15x15 bundle onward. ....	59
41.	MCNP simulated energy deposited per fiber in a 1x1, 2x2, 3x3, 4x4, 5x5, 6x6, 7x7, 8x8, 9x9, 10x10, 15x15, 20x20, 40x40, and 100x100 fiber bundle (left to right, top to bottom). Lighter colors represent more energy deposited than darker colors. Note that the energy scale is identical to that of Figure 26. The location of the isotropic neutron source is defined by Part G of Figure 8. A noticeable gradient in energy deposition can be seen starting from the 20x20 bundle onward. Notice that more energy is deposited deeper inside the bundle compared to Figure 26. ....	60
42.	MCNP simulated energy deposited per fiber in a 1x1, 2x2, 3x3, 4x4, 5x5, 6x6, 7x7, 8x8, 9x9, 10x10, 15x15, 20x20, 40x40, and 100x100 fiber bundle (left to right, top to bottom). Lighter colors represent more energy deposited than darker colors. Note that the energy scale is identical to that of Figure 26. The location of the isotropic neutron source is defined by Part H of Figure 8. A noticeable gradient in energy deposition can be seen starting from the 40x40 bundle onward. Notice that less energy is deposited deeper inside the bundle compared to Figure 26. ....	61
43.	Representative waveform measured from the single fiber irradiated with Am-241. ....	62
44.	Representative waveform measured from the 7x3 fiber bundle irradiated with Am-241. ....	62
45.	Representative waveform measured from the single fiber irradiated with Cs-137. ....	63



Figure	Page
46.	Representative waveform measured from the 7x3 fiber bundle irradiated with Cs-137..... 63
47.	Distributions of peak separation times measured during Cs-137 irradiation of single fiber and 7x3 fiber bundle. .... 64
48.	Distributions of number of peaks measured during Cs-137 irradiation of single fiber and 7x3 fiber bundle. .... 65
49.	Distributions of number of peaks measured during Am-241 irradiation of single fiber and 7x3 fiber bundle. .... 65
50.	Distributions of peak separation times measured during Am-241 irradiation of single fiber and 7x3 fiber bundle. .... 66

## List of Tables

Table		Page
1.	BCF-12 Fiber Properties [18]. . . . .	9
2.	Kinematics of neutron scattering variables. . . . .	12
3.	Maximum fractional energy transfer in neutron elastic scattering. . . . .	13
4.	Vertical acquisition specifications for the Tektronix DPO7104 digital oscilloscope used during this investigation. . . . .	20
5.	Horizontal acquisition specifications for the Tektronix DPO7104 digital oscilloscope used during this investigation. . . . .	21
6.	Radioactive sources used during dual-ended readout portions of this research. . . . .	38
7.	Specifications of the CCD camera used during this investigation. . . . .	39
8.	Dark current and light leakage counts for the three dark configurations used in this investigation. . . . .	47
9.	Dark current and light leakage counts for the three dark configurations used in this investigation. . . . .	49
10.	Mean voltage pulse values for scintillation events in a single BCF-12 scintillating fiber. . . . .	53
11.	Mean voltage pulse values for scintillation events in a 7x3 bundle of BCF-12 scintillating fibers. Note the increase in mean voltages compared to the values in Table 10. . . . .	53

## List of Abbreviations

Abbreviation		Page
SNM	special nuclear material . . . . .	1
UAVs	unmanned aerial vehicles . . . . .	1
PMTs	photomultiplier tubes . . . . .	1
CCD	charge coupled device . . . . .	1
NaI	sodium iodide . . . . .	3
MeVee	MeV electron equivalent . . . . .	7
FHWM	full width at half maximum . . . . .	8
PVT	polyvinyl toluene . . . . .	8
PMMA	polymethyl methacrylate . . . . .	8
EMA	Extra Mural Absorber . . . . .	9
SCA	single channel analyzer . . . . .	17
MCA	multichannel analyzer . . . . .	17
VISA	Virtual Instrument Software Architecture . . . . .	19
MCNP	Monte Carlo N-Particle . . . . .	23
COTS	commercial off-the-shelf . . . . .	39
FOV	field of view . . . . .	40

# INVESTIGATION OF BCF-12 PLASTIC SCINTILLATING COHERENT FIBER BUNDLE TIMING PROPERTIES

## I. Introduction

### 1.1 Background

Fundamental problems with detecting large quantities of special nuclear material (SNM) at ranges of only a few kilometers remain a national security concern. Nuclear proliferation and the threat of nuclear terrorism continue to grow at alarming rates. Consequently, the need for monitoring of illicit nuclear trafficking has become increasingly important. Detection of SNM neutron radiation at standoff ranges ( $\geq 1$  km) requires the capability to both spectroscopically identify and estimate its spatial location based on the observation of very few neutron scattering events. Present methods rely on cumbersome and inefficient technologies which make them impossible to implement on remote sensing platforms such as unmanned aerial vehicles (UAVs) which could patrol border crossings and shipping lanes. A reasonable remote detector must be reliable, compact, efficient, and be able to discern and extract signal information from a heterogeneous radiation environment. By using a bundle of thin fiber scintillators optically coupled to both photomultiplier tubes (PMTs) and charge coupled device (CCD) cameras, an efficient neutron detector with inherent particle tracking spatial resolutions can be attained. The use of thin fibers allow neutrons to scatter, depositing energy and escaping one fiber potentially depositing energy in another fiber, allowing for tracking of incident neutron energy and direction.

## 1.2 Objectives

The objective of this research is to investigate the timing properties of BCF-12 scintillating plastic fibers arranged in a coherent bundle. Investigating these bundles is a critical first step in the development of a novel time-of-flight neutron detector. BCF-12 fibers are studied because of their fast time response, peak wavelength of emission, and their sensitivity to neutrons. These fibers are optically coupled to PMTs at both ends for a dual-ended readout technique using digital pulse processing to investigate the scintillation pulse shapes, spatial resolution of the fibers, and the suppression of noise. The interactions of neutrons with fiber bundle geometries are simulated to investigate the physics of neutron scattering in multiple fibers. Results from simulations and empirical measurements are described and discussed in this work.

## 1.3 Thesis Outline

This thesis presents some background information related to, the objectives of, and the methodology to be applied to my thesis research. It is divided into the following chapters: Chapter II - theory and background associated with the problem; Chapter III - experiments performed during this investigation; Chapter IV - experimental results and analysis; and Chapter Chapter V - conclusions and recommendations for future work. Chapter II discusses the background information relevant to scintillation detection, neutron kinematics, scintillating fiber materials of interest, photomultiplier tubes, and the concepts behind digital data acquisition. Chapter III discusses the experimental and computational objectives to include the methodology, tools, and equipment to be used in accomplishing them. Chapter IV presents the results of the experiments performed during this investigation. Chapter V summarizes the research performed and provides recommendations for future fiber bundle work.

## II. Theory

### 2.1 Overview of Scintillators

Radiation detection using scintillation light produced in special materials is one of the oldest techniques used in nuclear engineering today. Such scintillation materials should be able to convert the kinetic energy of incident particles into detectable light with reasonable efficiency. The conversion of kinetic energy to light yield should also be linearly proportional to the energy deposited over a wide range. The scintillating material should have good optical characteristics; it should be transparent to the wavelength of its own emission and its index of refraction should be close to glass to allow efficient coupling of the scintillation light to light sensor being used (typically a PMT).

There are two types of scintillators: inorganic and organic. Inorganic scintillators in the form of alkali halide crystals, notably sodium iodide (NaI) crystals, are the most widely used. Inorganic scintillators typically have the largest light output and superior linearity but have the disadvantage of a slow response time. The constituent atoms of inorganic materials typically have a high density and Z-value which makes them the ideal choice for gamma-ray spectroscopy. Organic scintillators generally have a faster response time but a lower light yield than inorganic scintillators. Organic scintillators are commonly used for neutron detection and beta spectroscopy because of the prevalence of hydrogen in organic materials.

The light produced during a scintillation event comes from three mechanisms: fluorescence, phosphorescence, and delayed fluorescence. Fluorescence is the prompt emission of visible radiation following excitation with a decay approximately equal to the lifetime of the an excited singlet state (between  $10^{-9}$  and  $10^{-7}$  sec). Phosphorescence involves a transition to the excited triplet state with no return to the excited

singlet state. The decay in phosphorescence is approximately equal to the lifetime of the triplet state (between  $10^{-4}$  and 10 sec). Delayed fluorescence has the same emission spectrum as prompt fluorescence, but has an emission time that is only a bit shorter than phosphorescence. The delay is caused by a brief transition from the excited singlet state to the triplet state and back to the excited singlet state. A standard way to represent these quantum mechanical state transitions is in a Jablonksi plot, as seen in Figure 1. Scintillators that can convert a large proportion of the

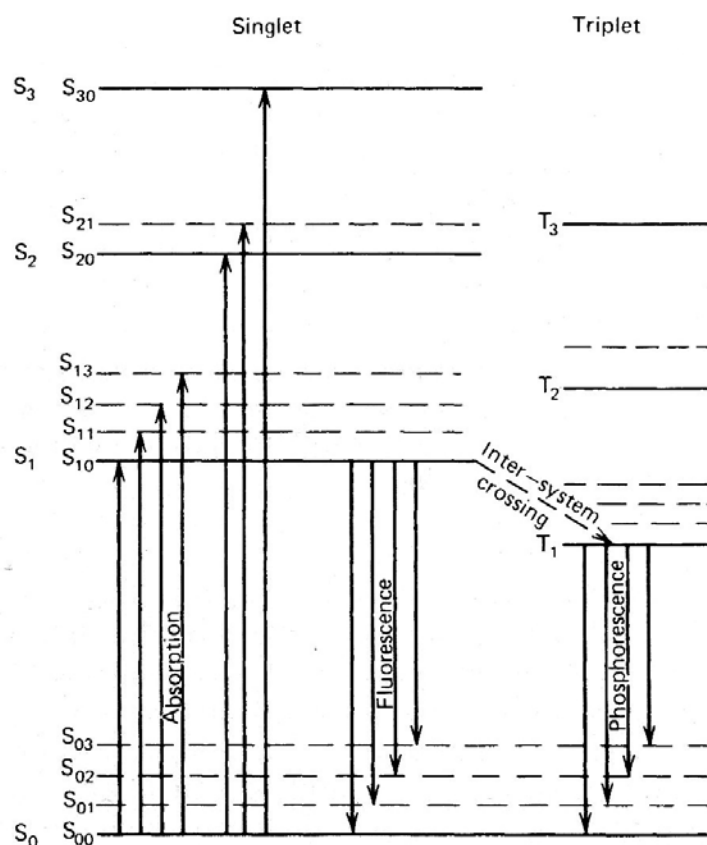


Figure 1. Jablonksi diagram of an organic molecule with  $\pi$ -electron structure [3].

incident radiation energy to prompt fluorescence while also minimizing contributions from phosphorescence and delayed fluorescence are typically used in radiation de-

tection. Scintillators used in pulse mode operation are primarily limited to prompt fluorescence because the pulse shaping times (for example, from fast PMTs) are much shorter than typical phosphorescence and delayed fluorescence times. The photons produced by these long-lived process are spread out between signal pulses caused by prompt fluorescence and can be thought of as noise.

## 2.2 Scintillation Mechanisms in Organics

Organic scintillator fluorescence occurs from energy level transitions in an organic molecule. For a given molecular species, fluorescence can be observed independent of its physical state; e.g. a solid, a vapor, or part of a solution. As a comparison, inorganic scintillators like NaI require a regular crystalline lattice as a foundation for the scintillation process. Many organic scintillators are based on organic molecules with a  $\pi$ -electron structure. As seen in Figure 1, energy can be absorbed by exciting the electron configuration into any one of the excited states. Singlet states (spin 0) are labeled with  $S$  and triplet (spin 1) states are labeled with  $T$ . Molecules that are part of organic scintillators have an energy spacing of between 3 and 4 eV from the  $S_0$  to the  $S_1$  states. Energy spacing between states above  $S_1$  being somewhat smaller than 3 eV. Each of these electronic states are subdivided into energy states with much finer spacing that match various vibration states of the molecule. Spacing between these vibrational levels is of the order of 0.15 eV, much higher than average thermal energies (0.025 eV). Because of this, practically all molecules are in the lowest vibrational state,  $S_{00}$ . When an incident particle passing by the organic scintillator molecule deposits kinetic energy, the higher singlet electronic states are excited quickly (on the order of picoseconds) and then de-excited to the  $S_1$  electron state via internal conversion. Internal conversion processes don't emit any radiation. Any state that has excess vibrational energy quickly loses that energy when reaching thermal equilibrium. The



net effect of excitation is, after a relatively short amount of time, a population of excited molecules in the  $S_{10}$  level. Prompt fluorescence scintillation photons are emitted in transitions between the  $S_{10}$  state and the vibrational states of the ground electronic state. If  $\tau$  represents the fluorescence decay time for the  $S_{10}$  level (usually a few nanoseconds for organic scintillators), the prompt fluorescence intensity at time  $t$  following excitation follows Equation 1.

$$I = I_0 e^{-t/\tau} \quad (1)$$

From Figure 1 it can be seen how organic scintillators are transparent to their own fluorescence emission. Because all fluorescence transitions have a lower energy than the minimum required for excitation, known as the *Stokes shift*, there is little self-absorption of the fluorescence photons. Scintillation efficiency is defined as the fraction of all of incident particle energy converted into visible light. An effect called *quenching* encompasses all de-excitation processes that are radiation less. Impurities such as dissolved oxygen in liquid scintillators can degrade the light output by serving as a quenching mechanism for excitation energy.

### 2.3 Light Output of Organic Scintillators

Most of the kinetic energy lost by a particle incident upon a scintillation material is dissipated nonradiatively in the form of heat. The fraction of particle energy converted to light, the scintillation efficiency, depends on the type of particle and its energy. For organic scintillators the response to electrons is linear up to energies of about 125 keV [4]. Heavy charged particles, such as alpha particles and protons, always have a smaller response when compared to electrons of the same energy. The response to heavy charged particles shows non-linearity up to larger energy thresholds

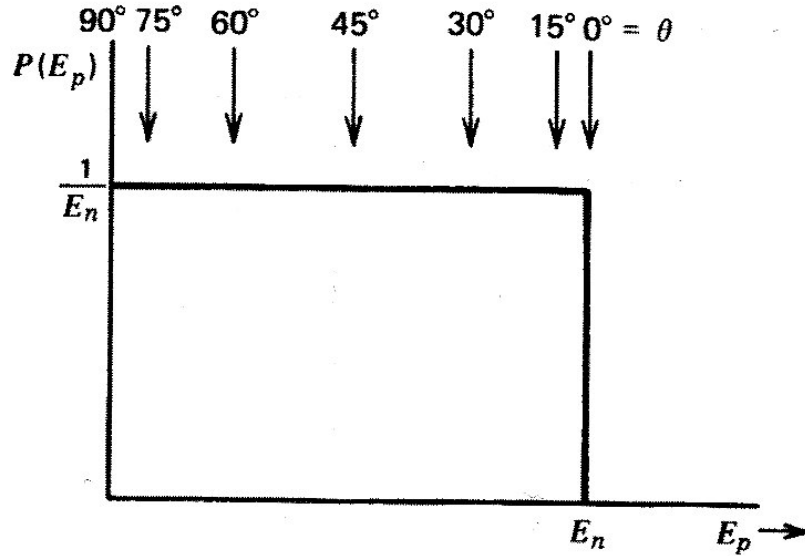


Figure 2. Energy distribution of recoil protons  $E_p$  produced by monoenergetic neutrons. For scattering from hydrogen,  $E_p$  is equivalent to  $E_R$  [9].

when compared to electrons [9]. For example, at a few hundred keV, the response to protons is an order of magnitude smaller compared with the light yield of equivalent energy electrons [15]. As energies increase the discrepancy is less, but the proton response is always below the electron response. A specific nomenclature to be used to describe absolute light yield in organic scintillators. The MeV electron equivalent (MeVee) is introduced to situate light yield on an absolute basis. The energy required to generate 1 MeVee of light by definition is 1 MeV for fast electrons and several MeV for heavy charged particles because of their reduced light yield per energy.

## 2.4 Time Response of Organic Scintillators

Assuming that the fluorescent states in an organic molecule are formed instantaneously and only prompt fluorescence is observed, then the time profile of the light pulse should be a very fast leading edge followed by a simple exponential decay as in Equation 1. However, the time it takes to populate the fluorescent states and the slower components of scintillation such as phosphorescence and delayed fluorescence

need to be taken into account. It takes approximately half a nanosecond to populate fluorescent state levels [13]. The decay time from these states is only three to four times greater for very fast scintillators [2]. There are two approaches that take into account this finite rise time. First, it is assumed that the population of the fluorescent states is also exponential ([10] and [14]) and the overall shape of the light pulse is given by Equation 2:

$$I = I_0(e^{-t/\tau} - e^{-t/\tau_1}) \quad (2)$$

where  $\tau$  is the time constant describing the decay of the fluorescent states and  $\tau_1$  describes the population of those states. The second approach [16] to describing the population of the fluorescent states is to conclude that the population step is better represented by a Gaussian function with a standard deviation  $\sigma_{ET}$ . The overall light versus time profile is then described by Equation 3.

$$I = I_0 \frac{1}{\sqrt{2\pi\sigma^2}} e^{-\frac{(x-\mu)^2}{2\sigma^2}} e^{-t/\tau} \quad (3)$$

The rise and fall time of the light output can be experimentally characterized by the full width at half maximum (FWHM) of the resulting light curve. It has become commonplace to gauge the performance of very fast organic scintillators by their FWHM as well as their decay time [12].

## 2.5 BCF-12 Fiber Scintillators

Plastic scintillators are organic scintillators that are dissolved in a solvent and are polymerized. A solvent consisting of a styrene monomer in which an appropriate organic scintillator is dissolved is a common example of this practice [7]. Other examples of plastic matrices are polyvinyl toluene (PVT) and polymethyl methacrylate (PMMA) [8]. The fibers that will be used for this research are BCF-12 fibers from

Saint-Gobain Crystals, Inc. Their fibers consist of a polystyrene based core and a PMMA cladding. External Extra Mural Absorber (EMA) is often used to eliminate optical crosstalk. The scintillating core contains a combination of fluorescent dopants selected to produce the desired scintillation, optical and radiation-resistance characteristics. Often, one property is enhanced while another is mildly compromised. In small fibers (<0.5mm), the fluor concentration is increased, usually at the expense of light attenuation length [6]. Table 1 lists the pertinent properties for the fibers used in this research. Figure 3 diagrams what a typical round scintillating fiber is made of.

**Table 1. BCF-12 Fiber Properties [18].**

Core Material	Polystyrene
Core Refractive Index	1.60
Density	1.05
Cladding Material	Acrylic
Cladding Refractive Index	1.49
Cladding Thickness	3% of fiber diameter
Numerical Aperture	0.58
Trapping Efficiency	3.44% minimum
No. of H atoms per cc (core)	$4.82 \times 10^{22}$
No. of C atoms per cc (core)	$4.85 \times 10^{22}$
No. of electrons per cc (core)	$3.4 \times 10^{23}$
Radiation Length	42 cm
Emission Color	Blue
Emission Peak, nm	432
Decay Time, ns	2.7
1/e Length, m	2.2
No. of Photons per MeV	$\sim 8000$
Operating Temperature	$-20^{\circ} \text{ C to } +50^{\circ} \text{ C}$
Vacuum Compatible	Yes

PMMA is the standard cladding material for Saint-Gobain Crystals' fibers. It has a density of 1.2 g/cc and refractive index of 1.49. The refractive index of the

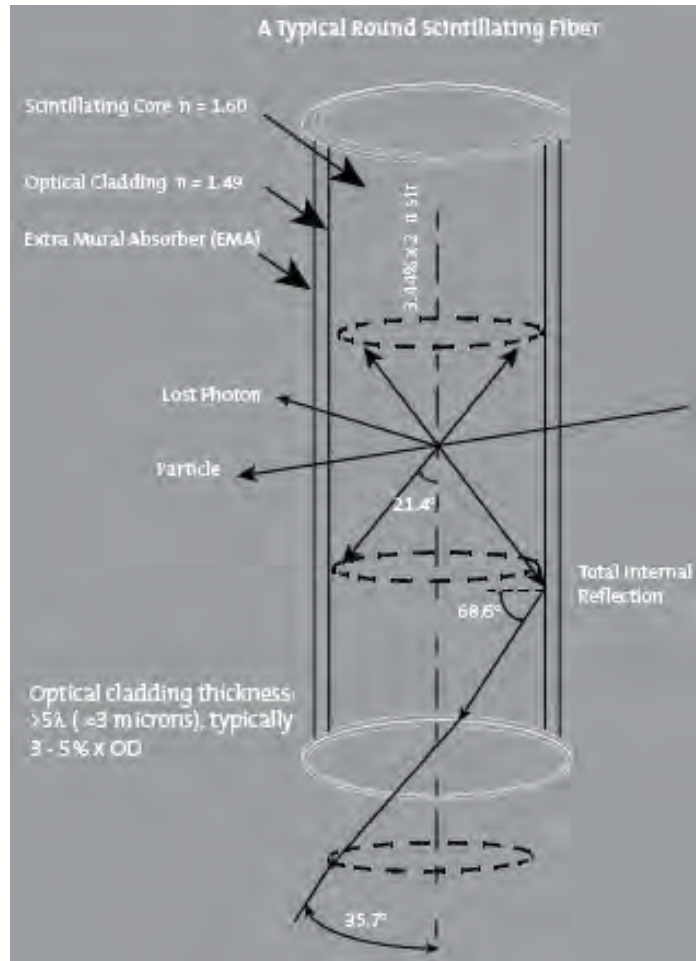


Figure 3. Diagram of typical Saint-Gobain scintillating fiber [18].

core and cladding and the cross section of the fiber determine the trapping efficiency. The trapping efficiency also depends on the distance between the fiber axis and the scintillation event. For Saint-Gobain fibers the trapping efficiency ranges from 3.4% for events occurring at the fiber axis to  $\sim 7\%$  for events near the core-cladding interface.

White or black coatings may be applied to the outer fiber surface primarily to eliminate crosstalk among closely packed fibers. Coatings are typically 10 to 15 microns thick. An EMA coating decreases the overall signal intensity obtained from a fiber, irrespective of its length. This effect is greatest with black EMA, as well as with short fibers. The coating can interfere with useful lightpiping in the cladding. Black EMA applied at the near end of fibers can be used to flatten out position dependent response. White EMA is used in the construction of short fiber imaging bundles.

## 2.6 Neutron Kinematics with Organic Scintillators

One of the most common methods of fast neutron detection is based on elastic scattering of neutrons by light nuclei such as hydrogen, deuterium, or helium [5]. A portion of the neutron's kinetic energy is transferred to the target nucleus resulting in a *recoil nucleus*. Hydrogen is by far the most popular target nuclei because it has the capability to transfer all of the incident neutron energy to it as seen in Table 3. When the target nuclei are light, the recoil nucleus behaves much like a proton or alpha particle in the way that it loses energy in the detector medium [17].

The values in Table 3 can be derived from four simple kinematic equations [11]. These equations use the variable definitions listed in Table 2 which are graphically represented by Figure 4. For incoming nonrelativistic neutrons ( $E_n \ll 939$  MeV), conserving momentum and energy in the center-of-mass coordinate frame give the

**Table 2. Kinematics of neutron scattering variables.**

Symbol	Definition
$A$	mass of target nucleus/neutron mass
$E_n$	incoming neutron kinetic energy in laboratory system
$E_R$	recoil nucleus kinetic energy in laboratory system
$\Theta$	scattering angle of neutron in center-of-mass coordinate system
$\theta$	scattering angle of recoil nucleus in the laboratory coordinate system

relation for the energy of the recoil nucleus given by

$$E_R = \frac{2A}{(1+A)^2}(1 - \cos \Theta)E_n. \quad (4)$$

To convert to the laboratory coordinate system, where the target nucleus is at rest, uses the transformation

$$\cos \theta = \sqrt{\frac{1 - \cos \Theta}{2}}. \quad (5)$$

Combining Equations 4 and 5 gives the relation for the recoil nucleus energy in terms of its own angle of recoil,

$$E_R = \frac{4A}{(1+A)^2}(\cos^2 \theta)E_n. \quad (6)$$

From Equation 6 it can be seen that the energy transferred to the recoil nucleus is determined by the scattering angle. If  $\theta \cong 90^\circ$ , then the recoil energy is near zero. However, a head-on collision between the incident neutron and target nucleus leads to a recoil in the same direction,  $\theta \cong 0^\circ$ , resulting in a maximum possible recoil energy as seen in Equation 7.

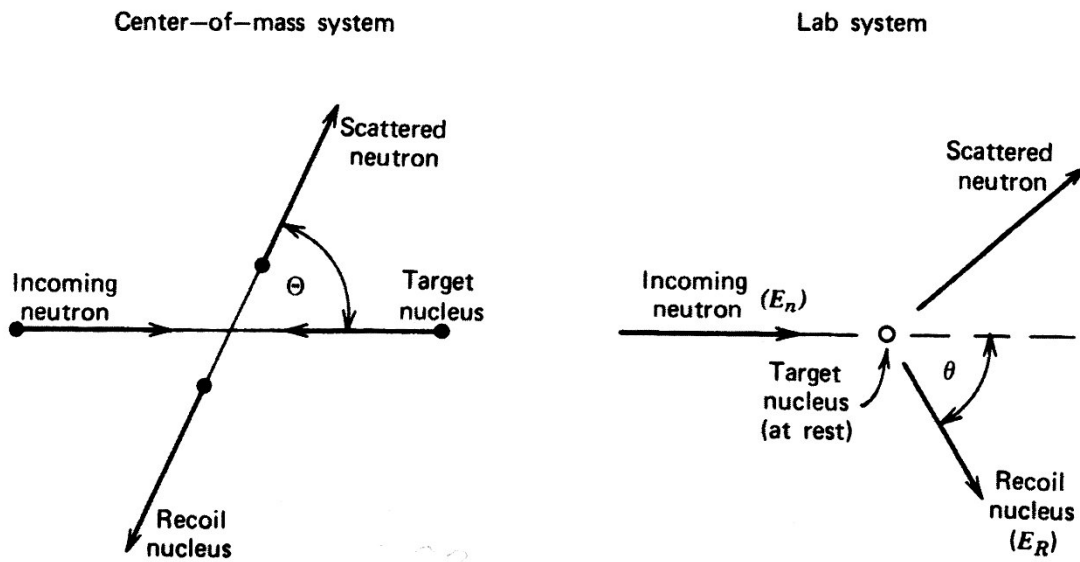
$$E_R|_{max} = \frac{4A}{(1+A)^2}E_n \quad (7)$$

Table 3 lists the maximum fraction of incoming neutron energy that can be trans-

ferred to a recoil nucleus for various target nuclei. As expected, the maximum fractional energy transfer decreases as the nucleus mass increases. This trend explains why hydrogen assumes the predominant role in neutron detection using elastic scattering.

**Table 3. Maximum fractional energy transfer in neutron elastic scattering.**

Target Nucleus	A	$\frac{E_R}{E_n} _{max}$
${}^1_1H$	1	1
${}^2_1H$	2	0.889
${}^3_2He$	3	0.750
${}^4_2He$	4	0.640
${}^{12}_6C$	12	0.284
${}^{16}_8O$	16	0.221



**Figure 4. Neutron kinematics [9].**

The energy distribution of recoil nuclei are distributed between a minimum of zero and a maximum value given in Table 3. Supposing all scattering angles are allowed,



a continuum of recoil energies between these two extremes is expected. If  $\sigma(\Theta)$  is defined as the differential cross section in the center-of-mass system, the probability that the neutrons will be scattered into  $d\Theta$  about  $\Theta$  is given by Equation 8,

$$P(\Theta)d\Theta = 2\pi \sin \Theta d\Theta \frac{\sigma(\Theta)}{\sigma_s} \quad (8)$$

where  $\sigma_s$  is the total scattering cross section integrated over all angles. However, the distribution in recoil nucleus energy is more informative than the distribution in recoil nucleus scattering angle. Because  $P(E_R)dE_R$  represents the probability of creating a recoil with energy in  $dE_R$  about  $E_R$ . This leads to Equation 9, which after substituting into Equation 8, gives Equation 10.

$$P(E_R)dE_R = P(\Theta)d\Theta \quad (9)$$

$$P(E_R) = 2\pi \sin \Theta \frac{\sigma(\Theta)}{\sigma_s} \cdot \frac{d\Theta}{dE_R} \quad (10)$$

Equation 10 shows that the expected recoil energy continuum has the same shape as the differential cross section  $\sigma(\Theta)$  as a function of the center-of-mass scattering angle for the incident neutron. The shape of  $\sigma(\Theta)$  tends to favor forward and backward scattering for most target nuclei. For a hydrogen nucleus, the scattering process is isotropic in the center-of-mass coordinate system. The expected proton recoil energy distribution is a rectangle extending from zero to the total energy of the incident neutron. A detector based on neutron-hydrogen scattering should have response function that matches this rectangular shape, as seen in Figure 2.

## 2.7 Photomultiplier Tubes

A photomultiplier tube serves two purposes: the conversion of photons into photoelectrons and the multiplication of said photoelectrons. Conversion of photons into photoelectrons occurs at the photocathode. The spectral response of a PMT is determined by both the PMT window material and the photocathode material. The photocathode in a PMT converts incident light energy into photoelectrons with the efficiency of this conversion depending on the wavelength of the incident light. The sensitivity of the PMT can be documented using either the quantum efficiency or the cathode radiant sensitivity. The sensitivity at long wavelengths is primarily limited by a reduction of light absorption by the photocathode and the relatively low energy imparted to the photoelectron. At shorter wavelengths the window material becomes the dominant factor in PMT sensitivity.

The time characteristics of a PMT are determined exclusively by the electron trajectories because the time required for photoemission is very short. The electron transit time of a PMT is the average time difference between the photon arriving at the photocathode and the burst of electrons at the anode. An important quantity when characterizing PMT timing characteristics is the spread in the electron transit time. This value is important because it determines the time width of the pulse of electrons arriving at the anode. The distance between the photocathode and first dynode is a major factor in the observed spread in transit time.

The shape of the voltage pulse produced at the anode of a PM following a scintillation event depends on the time constant of the anode circuit. Two extremes can occur; one where the time constant is very large compared to the decay time of the scintillator and one where the anode time constant is much smaller than the decay time of the scintillator. This is illustrated in Figure 5.

When the anode time constant is very large you get response from the PMT as

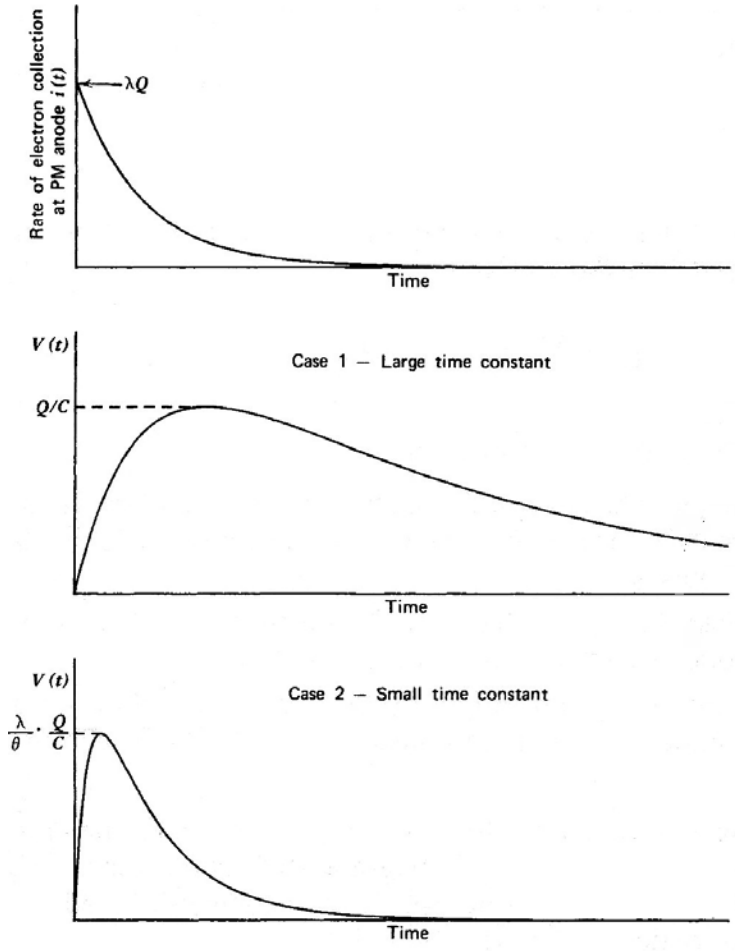


Figure 5. Plots of anode pulse for the two extremes of large and small anode time constant [9].

seen at the bottom of Figure 6. The PMT fully integrates all the light from the scintillator which comes out in discrete pulses as see in the middle of Figure 6. If the system response of the PMT is well-known, then deconvolution techniques may be used to extract timing information at the level of individual scintillation events.

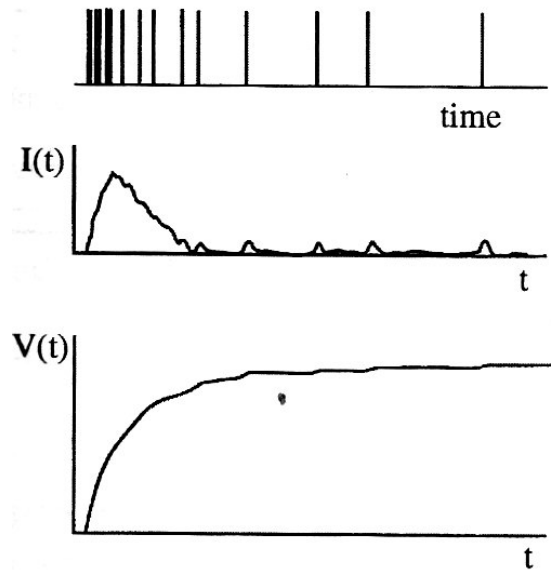


Figure 6. Top: Individual electrons leaving photocathode. Middle: Current at anode after transit through multiplying structure. Bottom: Leading edge of voltage pulse across anode circuit with long time constant. [9].

## 2.8 Digital Data Acquisition

Digital data acquisition is a powerful technique that replaces many of the pulse-shaping electronics commonly used in a nuclear engineering laboratory such as a preamplifier, linear amplifier, single channel analyzer (SCA), and multichannel analyzer (MCA). Raw pulses measured directly from the detector on an oscilloscope can be stored digitally for further post-processing. Once the raw data is saved, the behaviors of analog pulse-shaping electronics can be implemented via data processing

algorithms written in computer programming languages such as Fortran or C++, as well as scripting languages like MATLAB or Mathematica.

Digital data acquisition can bypass complications caused by connecting through several different analog pulse-shaping electronics. For example, some timing information is lost when measuring very fast events from a detector as it passes through a preamplifier and a linear amplifier. As the signal propagates through each of these pulse-shaping electronics, more and more noise is added at each step. This noise adds to uncertainty in time measurements. The shortest, least complicated path for signal propagation will allow for the most unambiguous measurements from any detector.

In the case of measuring scintillation events, one can measure directly from the dynode or anode of the PMT being used. This output can then be connected directly to a fast digital oscilloscope such as the Tektronix DPO7104 as seen in Figure 7. Specifications for the Tektronix DPO7104 can be found in Tables 4 and 5. The

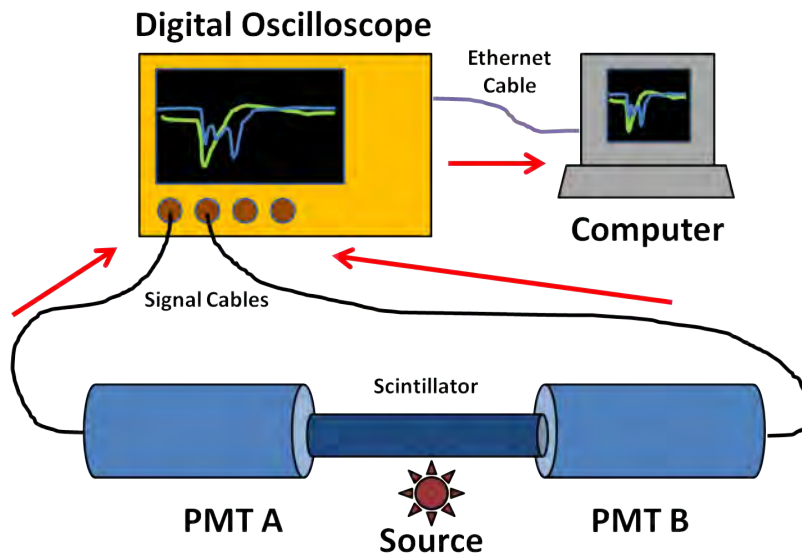


Figure 7. Diagram of dual-ended PMT readout using digital data acquisition. The light output from the scintillator is converted to voltage pulses by the PMTs, which are then measured by the digital oscilloscope. The oscilloscope captures a set number of waveforms digitally to its buffer followed by transferring the buffer to the computer via a gigabit Ethernet connection.

DPO7104 has three advantages that make it ideal for digitally acquiring fast signal pulses. The first advantage is its speed. It has a maximum sample rate of 20.0 GHz, meaning it has a time resolution that can get as low as 200 ps per datapoint. The second advantage is its FastFrame acquisition capability. With FastFrame acquisition, thousands of individual waveforms per second can be measured and stored in the oscilloscope's memory. The only limitation is the size of the oscilloscope memory and its sampling rate. The third advantage when using a DPO7104 oscilloscope is the ability to manipulate every setting on the oscilloscope through Virtual Instrument Software Architecture (VISA) commands. Popular laboratory data acquisition programs like MATLAB and LabView both have built in VISA interfaces compatible with the DPO7104. MATLAB also has instrument drivers that can be used to directly control instruments like the DPO7104 oscilloscope. However, MATLAB instrument drivers are not available for every instrument; user-created drivers can be notoriously unstable and prone to data corruption. The VISA interface is independent of instrument drivers and works as long as both the controller (e.g. MATLAB) and the instrument (e.g. Tektronix DPO7104) are VISA compliant. An advantage to using the VISA interface to digitally acquire data from an oscilloscope, like the DPO7104, is the capability to control every feature of the oscilloscope as if one were manually measuring signals on the oscilloscope. For example, it typically takes manual adjustment of settings like the voltage scale, time scale, resolution, trigger settings, and waveform positioning to get the oscilloscope to display all of the pertinent features of a waveform of interest. Once these settings are "dialed-in" manually, the equivalent VISA commands can be programmed into a MATLAB script to call up these settings any time they may be needed. Small adjustments like voltage scale or trigger level can easily be adjusted this way depending on changing experimental conditions such as using a different source or detector material.

**Table 4. Vertical acquisition specifications for the Tektronix DPO7104 digital oscilloscope used during this investigation.**

Input Channels	4
Bandwidth	1 GHz
Rise Time 10% to 90% (Typical)	300 ps
Rise Time 20% to 80% (Typical)	200 ps
DC Gain Accuracy	$\pm 1\%$ with offset/position set to 0
Bandwidth Limit	2.0 GHz
Input Coupling	AC, DC, GND
Input Impedance	$1\text{ M}\Omega \pm 1\%$ with $13\text{ pF} \pm 2\text{ pF}$ , $50\Omega \pm 1\%$
Input Sensitivity	$1\text{ M}\Omega$ : 1 mV/div to 10 V/div $50\Omega$ : 1 mV/div to 1 V/div
Vertical Resolution	8 bit ( $> 11$ bit with Hi Res)
Max Input Voltage, $1\text{ M}\Omega$	150 V CAT I, derate at 20 dB/decade to $9 V_{RMS}$ above 200 kHz
Max Input Voltage, $50\Omega$	$5V_{RMS}$ , with peaks $\leq \pm 24\text{ V}$
Position Range	$\pm 5$ divisions
Delay between any Two Channels	$\leq 100\text{ ps}$ ( $50\Omega$ )

The Tektronix DPO7104 used in this research saves all waveform data internally as signed 8-bit integers ranging from -128 to +127. Then, depending on the voltage scale chosen, a conversion factor is needed to convert from these integer data values to actual voltages. This highlights a disadvantage of using a digital oscilloscope such as the DPO7104. The fidelity of voltage measurements is limited by the chosen voltage scale as well as the requirement that any pertinent waveform data fit within the voltage window and time window of the oscilloscope. When taking measurements one should keep in mind that voltage data points will always be separated by *at least* the voltage window range divided by 256 (for 8-bit oscilloscopes).

To maximize the digital measurement capabilities of the oscilloscope, two groups of settings need to be adjusted. First, the baseline of a negative polarity pulse needs to be set as close to the top of the voltage window as possible without cutting off any

**Table 5. Horizontal acquisition specifications for the Tektronix DPO7104 digital oscilloscope used during this investigation.**

Maximum Sample Rate (1 ch)	20GS/s
Maximum Sample Rate (2 ch)	10GS/s
Maximum Sample Rate (3-4 ch)	5GS/s
Maximum Equivalent Time Sampling Rate	4 TS/s
Maximum Record Length with Standard Configuration	50M (1 ch), 25M (2 ch), 12.5M (3-4 ch)
Time Base Range	50 ps/div to 1000 s/div
Time Resolution (in ET/IT mode)	500 fs
Time Base Delay Time Range	5 ns to 250 s
Trigger Jitter (RMS)	1.5 ps <sub>RMS</sub> with enhanced triggering OFF <100 fs <sub>RMS</sub> with enhanced triggering ON
Maximum FastAcq Waveform Capture Rate	>250,000 wfms/s on all 4 channels simultaneously
FastFrame Acquisition	Acquisition memory divided into segments; maximum trigger rate >310,000 waveforms per second. Time of arrival recorded with each event. Frame Finder tool helps to visually identify transients



relevant positive polarity portions of the waveform. This allows for the entire range of the voltage window to be used in measuring the pulse voltage (using all 8-bits). Second, a balance between the time resolution and number of data points needs to be struck. In other words, one should keep the number of data points large enough to describe the waveform being studied with good statistics but not so large as to not be able to resolve very fast (e.g. sub-nanosecond) features in the waveform.

When connecting detectors directly to the DPO7104 oscilloscope, an RG-58 C/U BNC cable should be used because of its characteristic impedance of  $50\ \Omega$ . The oscilloscope can be set to accept an input impedance of  $1\ \text{M}\Omega$  or  $50\ \Omega$ . The  $1\ \text{M}\Omega$  setting should be used only if the cable being used is terminated with a resistor that matches its impedance. For example, an RG-62 cable would need to be terminated with a  $93\ \Omega$  resistor. Using  $50\ \Omega$  cables and setting the oscilloscope input impedance to  $50\ \Omega$  negates the need for any terminator resistors.

### III. Methodology

#### 3.1 Simulation of Neutron Radiation on Fiber Bundles

A Monte Carlo N-Particle (MCNP) transport model was developed with the objective of analyzing the interaction of neutrons with fiber bundles of varying size. Fourteen fiber bundles were modeled with dimensions as follows: 1x1, 2x2, 3x3, 4x4, 5x5, 6x6, 7x7, 8x8, 9x9, 10x10, 15x15, 20x20, 40x40, and 100x100. The fibers were modeled with a diameter of 500 microns and a fiber spacing of 5 microns, to match the size of the cladding. The space between the fibers, as well as the space encompassing the entire fiber bundle and source location, was modeled as a perfect vacuum. The fibers were modeled as a bare styrene ( $C_6H_5CH=CH_2$ ) core without the cladding. A 2.5 MeV, isotropic neutron source was modeled and placed at different locations relative to the fiber bundle. Five million source particles were simulated. The different source locations are shown in Figure 8.

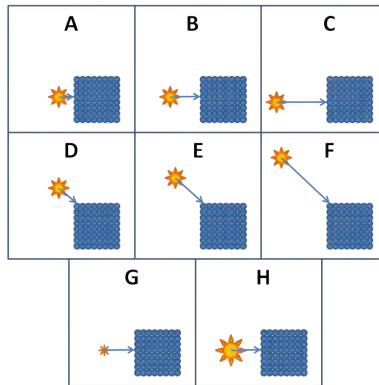


Figure 8. Different arrangement of source and fiber bundle in the MCNP simulations. Parts A, B, and C show the source increasing in distance (5, 10, and 20 cm) from the fiber bundle while staying centered longitudinally and vertically with the bundle. Parts D, E, and F show the source increasing in distance (5, 10, and 20 cm) from the top-left corner of the fiber bundle while staying centered longitudinally with the bundle. Parts G and H are identical to Part A, except the source is located at the far end and close end of the fiber bundle respectively.

MATLAB code was written to create the different MCNP input files with some variables entered by the the user, to include: the number of source particles, the source particle energy, the source location, the spacing between the fibers, and the number of fibers along the x- and y-axis. The fibers are always parallel to the z-axis. At the 2x2 fiber bundle size the MCNP input file has 34 total lines of code - a reasonable amount of lines to manually code by hand. However, the 100x100 fiber bundle input file has over 34,000 lines of code - a coding task better left to a computer. Although MCNP has the native capability to create repeated lattice structures such as a bundle of identical fibers, this capability could not be used for two reasons. First, each fiber needed to be identified by a unique cell number when using the particle track data. This is not possible when using a lattice framework in MCNP. Second, the spacing and material between the fibers is more difficult to control when using MCNP's lattice functionality. This second point is important if one should wish to model a free-air, widely spaced fiber bundle. Once the repeating nature of the fiber bundle geometry is well understood, it is relatively straightforward to develop MATLAB code that can create MCNP input files that model different sized fiber bundles while still allowing for each fiber to be individually addressed. Run times for creating the MCNP input files lasted between 1 and 30 seconds, while the simulation run times lasted between 1 to 29 minutes depending on the size of the bundle being processed.

MCNP was configured to output particle track information for all particles that entered the volume of any fiber in the bundle. MCNP would output the total history of these particles until they left the bundle completely. Fiber surface crossings and collisions with the carbon or hydrogen in the fiber were the two types of events recorded. At each of these events, the particle's position, direction, and energy were recorded. If it was a surface-crossing event, the surface it crossed was also recorded.

For collision events, the cell where the collision took place and the type of particle collision (hydrogen or carbon) was recorded along with the new energy of the particle.

MATLAB code was then developed to parse through the MCNP ASCII particle track files. These particle track files ranged in size from 1.4 MB for a 1x1 bundle to 8400 MB for a 100x100 bundle. This code parses out a list of collision events saving the type of collision (hydrogen or carbon), the fiber it occurred in, the energy deposited for that event, and the number of total scattering events for that an individual particle history.

### **3.2 Characterizing PMT Dark Counts and Light Leakage**

All PMTs have an intrinsic dark current as discussed in Chapter II. For PMTs that aren't sealed with a scintillating material during manufacturing, there is also the potential for stray external photons to reach the photocathode of the PMT if it isn't in a perfectly dark environment. It is important to identify and characterize both the dark current pulses and light leakage pulses so that they can be distinguished from the weak light pulses created by organic scintillators.

In order to measure only the pulses arising from a PMT's dark current, an absolutely dark environment needs to be created around the PMT's window. The first experiment to explore this involved using an aluminum can and collar as shown in Figure 9. A lens cap was placed in front of the PMT window before being sealed up with the aluminum collar and can. Additionally, electrical tape was triple-wrapped around the seam between the collar and can as well as around the tiny gap between the collar and PMT tube to prevent any stray light from reaching the photocathode. Next, one million waveforms were digitally acquired using the digital data acquisition setup described in Chapter II.

Another dark count experiment was designed in order to test the light-tight ef-

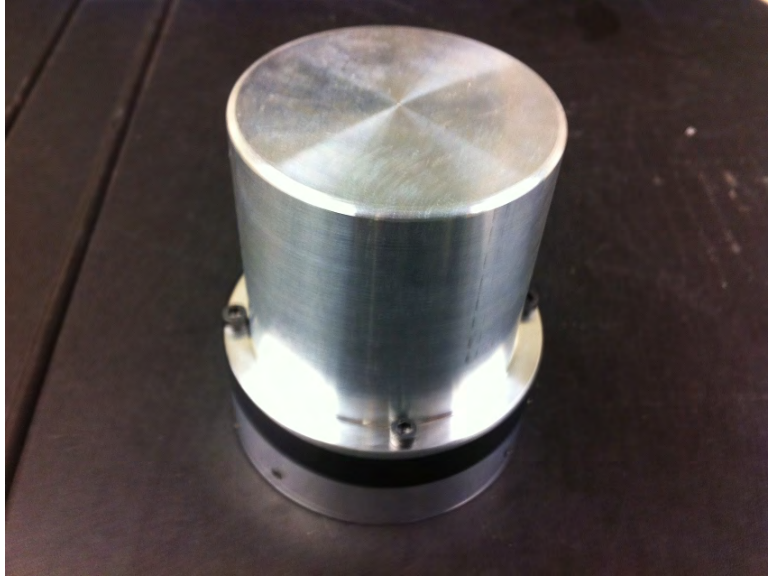


**Figure 9. Aluminum can and collar system. The collar attaches to the PMT tube via set screws. The aluminum can bolts to the collar. The can holds either the NaI crystal or the BC-404 bulk plastic scintillator. For the dark count experiment, the can was empty, no scintillating material was present. The can was used to cut down light leakage onto the PMT. Tape is wrapped around the seam between the collar and can. More tape is wrapped around the gap between the collar and the PMT tube.**

fectiveness of the large dark box seen in Figure 10. The large interior space of this dark box lends itself well to further experiments, provided it is sufficiently light-tight, because it can stage larger equipment configurations and longer fiber bundles. An experiment combining the dual-ended readout PMT setup with CCD cameras for imaging the fiber bundle is an example of one could take advantage of this large interior space. A bare PMT was placed inside the large dark box with the high voltage bias supply cable and signal cable connecting through the back wall of the dark box (as seen in Figure 11) to maintain the interior as light-tight as possible. A million waveforms were digitally acquired using this setup.

A similar setup to aluminum collar and can system was used to test whether or not dark pulses can be distinguished from scintillation pulses in “real-time” as they are being digitally acquired. A cylindrical piece of BC-404 scintillating plastic (as



Figure 10. Image of the large dark box used for three experiments during this investigation. It is designed to be water tight. Water tight doesn't mean light tight, as discovered over the course of this research.



Figure 11. Left: Interior BNC connections for two pairs of PMTs. Right: Exterior BNC connections for the PMTs inside the dark box. These connections allowed for the PMT bias and signal cables to be connected while keeping the box completely closed and sealed.

seen on the right side of Figure 12) was optically coupled to the PMT, instead of placing a lens cap in front of the PMT window - inside the aluminum can.



**Figure 12.** A picture of the bulk scintillator used during this investigation. The NaI scintillator is on the left and the BC-404 plastic scintillator is on the right. Electrical tape is wrapped around the plastic scintillator to prevent stray light from radially entering the scintillator medium. The end of the plastic scintillator not facing the PMT window is also blacked out for the same reason.

Before applying the optical grease, the PMT window was cleaned with isopropyl alcohol and air-dried. Bicon 6630-00001 optical grease was applied thinly across the face of the scintillating plastic before it was coupled to the PMT window. Another one million waveforms were digitally acquired using this setup.

The time necessary to acquire the one million waveforms in each of the experiments just described was recorded along with the waveforms themselves. Because the total number of acquisitions was the same from experiment to experiment, a longer acquisition time means the enclosure is doing a better job keeping stray photons away from the photocathode of the PMT. Total acquisition time gives a quantitative comparison of how light-tight a specific enclosure was.



### 3.3 Construction of Fiber Bundle

The material properties of the BCF-12 plastic scintillator fibers used in this research can be found in the Table 1. The first type of fiber bundle created was a 5x5 array with a 2.54mm air gap between fibers. To start, 25 fibers were fed through holes in two layers of perfboard and cemented to the perfboard with steel impregnated epoxy. The fibers were arranged vertically during the cementing step to prevent any permanent bending of the fibers after the epoxy had cured. The ends of the fibers were cleaved with a wire cutter. This type of fiber bundle can be seen in Figure 13.

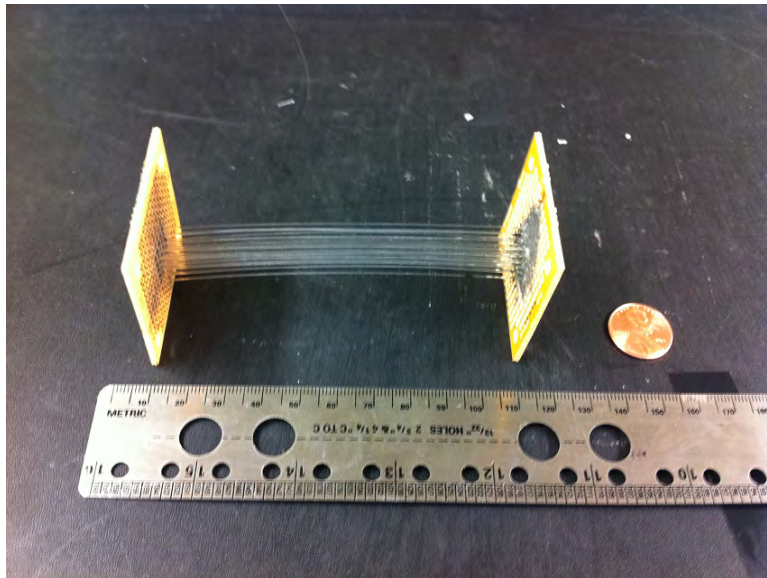


**Figure 13.** Image of first attempt at constructing a fiber bundle. The 25x25 bundle is framed by standard electronics perfboard. The fibers are cemented to the perfboard by a steel-impregnated binary epoxy. There is an 2.54 mm air gap between each fiber. Bending of the fibers is a noticeable drawback of this method of fiber bundle construction.

The first fiber bundle was abandoned for three reasons. First, it was difficult to cleanly apply the epoxy on the perfboard and between the fibers. The epoxy is sticky and often ended up several centimeters along the length of the fibers during



the epoxy application step. Second, the method of cleaving the fiber ends left them jagged - incapable of optically coupling to a PMT window. Third, even though effort was taken to keep the fibers taut, some of them still managed to relax during the cementing step - leaving a slight bow over the length of the fiber bundle.

The second type of fiber bundle created was a 7x3 array with no air gap between the fibers. First, a ribbon of seven fibers was laid down over plastic supports spaced about 2 inches apart from each other as seen in Figure 14. The ends of the ribbon were

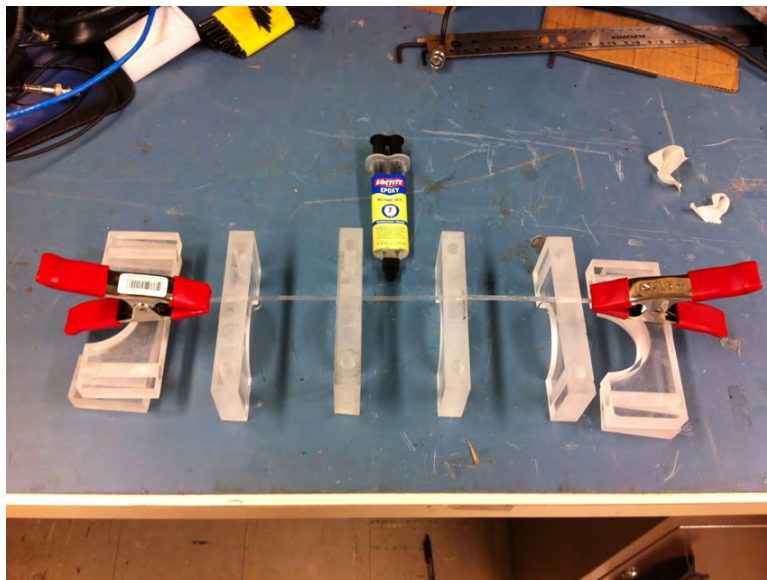


**Figure 14. Image of how the fiber ribbons were made. Fibers are held taut and clamped down at both ends. They are anchored to the four supports by double-sided tape. One-minute epoxy (shown at the top-middle of the image) is carefully applied to the fiber ribbon near the clamp ends and in the regions between the supports.**

held taut by clamps. Double-sided tape was used to temporarily fasten the ribbon to the plastic supports. After the ribbon was secured, Loctite 1-minute epoxy was applied with a brush along the fiber bundle between the gaps of the plastic supports. This epoxy was easier to work with and completely cured in about 4 hours. After that, a second and a third ribbon were made in the exact same manner. Next, the

three ribbons were joined together. A thin layer of epoxy was spread over the first ribbon and the second ribbon placed on top. The two ribbons were then clamped together and left to cure for about 4 hours. The third ribbon was epoxied to the first pair in the same way. Lastly, the fiber bundle ends were cleaved with a hot blade. The hot blade that was used was part of a soldering iron kit and can be seen in Figure 15. The advantage of a hot blade is its ability to cleave plastic fibers without the need



**Figure 15. Hot knife used to cleave ends of the fibers used during this investigation. The blade is adapted to attach to the end of a standard electronics soldering iron.**

for polishing afterward. A hot blade simultaneously polishes the fiber surface while cutting it [1]. See Figures 16 and 17 for the end result of the second fiber bundle construction method.

The second fiber bundle is superior to the first for three reasons. First, the fiber bundle is inherently more rigid because of how the fibers are epoxied to each other. Second, there is no bowing in the second fiber bundle as there was in the first. Third, the fiber bundle faces are more reliably cleaved and polished when compared to the

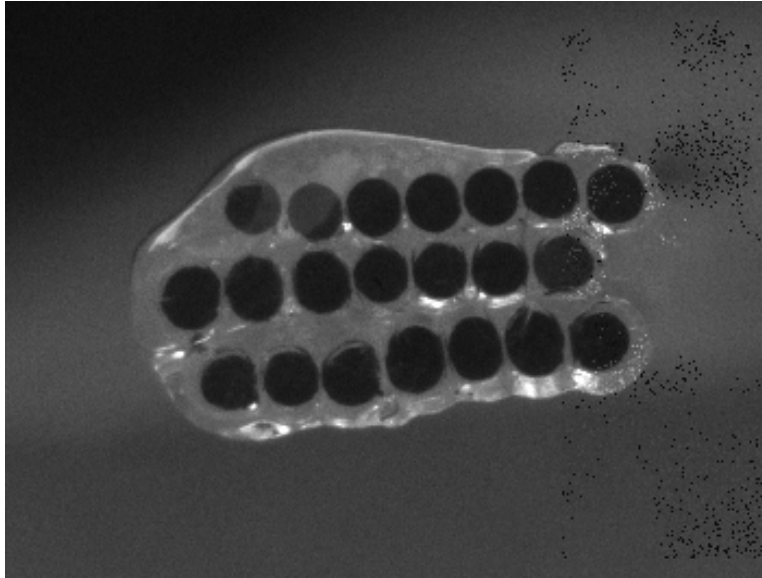


Figure 16. Face view of the fiber bundle taken with CCD camera with magnifying optics. Notice the close packing of the fibers in each row compared to the epoxy bulges separating the three layers. Also note how the top layer isn't lined up with the bottom two layers.

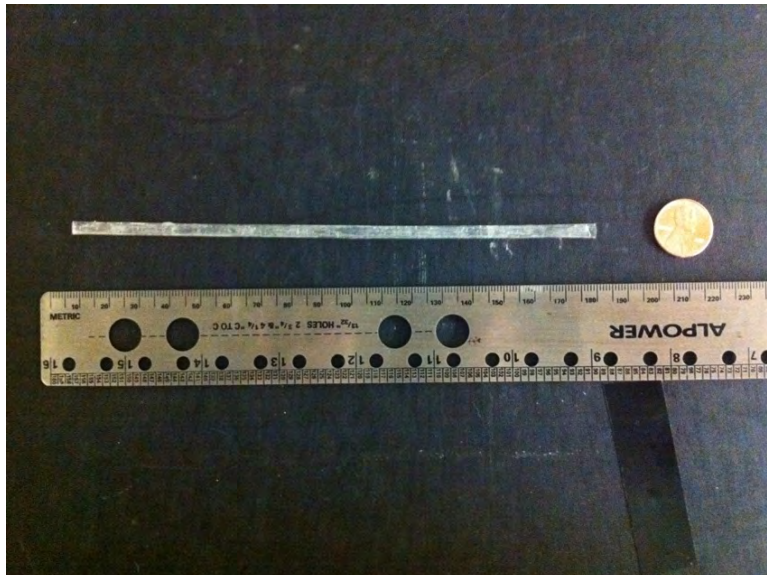


Figure 17. Image of the fully constructed 7x3, no air-gap fiber bundle. The bundle is 19 cm long. A close-up of the bundle face can be found in Figure 16.

first fiber bundle type. This will later allow for optical coupling with the PMT windows.

In general there are inherent complications when working with plastic fibers. One complication arises from getting an acceptable cleave of the fiber end. Sometimes the hot blade would pinch more than it would cut leading to a gradual shortening of the fiber bundle length as the perfect cut was sought. The individual fibers used in the 7x3 bundle started out at 30 cm while the bundle itself ended up at 19 cm. Figure 18 illustrates the wasted bits of fiber left over after finally getting an acceptable cleave of the fiber bundle.



**Figure 18.** Fiber scraps from left from botched attempts at cleaving individual fibers, fiber ribbons, and fiber bundles. The fibers that were used for the fiber ribbon construction started out at 30 cm. When constructed the fiber ribbons ended up at 25 cm. The final bundle measured in at 19 cm. The difficulty in getting a clean fiber cleave resulted in wasting 33% of the initial fiber length.

### 3.4 Dual-Ended Readout of Fibers

Measuring a scintillation light pulse simultaneously from both ends of a scintillating fiber can potentially be used to determine where the scintillation event took place along the length of the fiber. This kind of dual-ended readout is also useful in discriminating scintillation signals from a noisy background.

Before any data collection using two PMTs can take place, they need to be gain matched. Gain matching ensures that two PMTs will produce the same magnitude voltage pulse from the same amount of light collected. Six voltage pulse height spectra for each PMT used in this research were taken at high-voltage biases of 2.4, 2.5, 2.6, 2.7, 2.8, and 2.9 kV. The spectra were produced by the scintillation events from a NaI crystal irradiated with a Cs-137 radioactive source. For each spectrum, the channel number associated with the full energy peak of the 662 keV gamma ray of Cs-137 was recorded. As the gain increases, so does the channel number of the full energy peak. Because a linear relationship exists between gain and channel number, a least-squares fit gives a linear equation for channel number versus bias voltage for both PMTs. With these two equations, one PMT can arbitrarily be set to a certain bias, while the other is set to the bias that will produce the same response seen in the first PMT.

Three different dual-ended readout techniques were attempted during this investigation, although only one was used for actual data collection. The first and simplest technique used two bare PMTs connected inside the large dark box seen in Figure 10. The fiber bundle was sandwiched between the two PMT windows and both ends of the bundle were coated with optical grease to enhance the optical coupling between the fiber faces and PMT windows. This technique seemed to work well for the 7x3 fiber bundle but not for the lone fiber or the small 2x1 bundle. The 7x3 bundle had a natural rigidity that kept the fibers from bending when pinched between the



PMTs. The single fiber and 2x1 bundle tended to slip along the PMT window during handling of the dark box. This slipping is illustrated in Figure 19. It was discovered

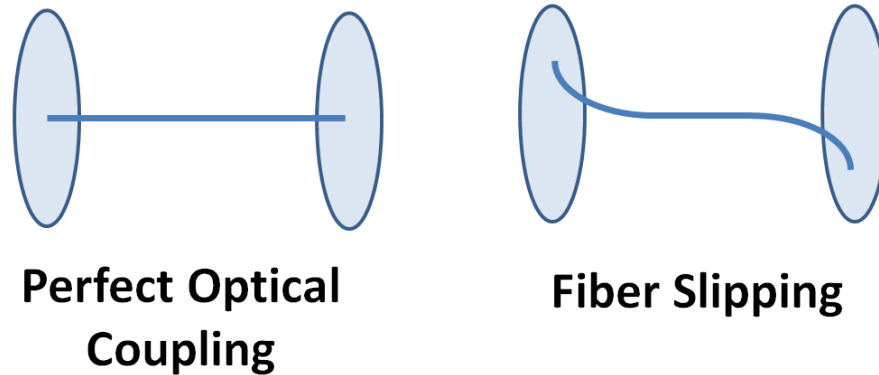


**Figure 19. Illustration of fiber slipping along the PMT window. If the fibers and PMTs are not anchored securely, then fiber slipping can occur. Fiber slipping is problematic for two reasons: the fiber face moves away from the center (most sensitive part) of the PMT window and light from the fiber face has a chance to skip across the PMT window without reaching the photocathode.**

during this attempt that both PMTs needed to be securely anchored to the dark box (after just enough compression was applied to the fiber bundle) to ensure the fibers did not slip during measurement.

This led to the second attempt at reliably acquiring dual-ended readout data. A cardboard box was triple-wrapped in electrical tape with an opening flap on top and circular holes cut on both ends of the box where PMTs could poke through. First, one PMT was secured in place with electrical tape so that its window was inside the cardboard dark box. Second, the fiber bundle was placed on a plastic stand inside the box and coupled with optical grease to the PMT. Next, the remaining PMT was inserted through the other end of the box, pinching the fiber bundle, and secured with electrical tape. The opening flap was sealed and the entire apparatus was placed inside the larger dark box as seen in Figure 20. This method temporarily solved the issue of fiber slipping until the temperature around the cardboard dark box



**Figure 20.** Image of the cardboard dark box. Electrical tape is triple-wrapped around all faces and edges of the box. Two holes are cut on opposite ends of the box to allow for insertion of the PMTs. A hatch is cut on the top of the box to allow for fiber bundle and radioactive source placement. The advantage of this design is it's darker than the larger plastic dark box used previously, while also being portable. The disadvantage of this design is the fragile nature of the tape adhesive. Changes in temperature made the tape peel off and loosen the PMTs from the box, resulting in fiber slipping.

increased beyond 87°F, the upper temperature limit of the tape's adhesive. This rise in temperature was caused by a combination of the heat created by the PMTs and an increase in laboratory temperature caused by a malfunctioning building heating and cooling system. The heat caused the tape to peel back and loosen the PMTs from the cardboard dark box. This caused the PMTs to move and allow the fiber bundle face to slip again.

The fragile nature of the cardboard dark box led to the design of an aluminum dark box with similar functionality. Six 1/4" thick aluminum sheets were cut to form the sides of the dark box. Two holes were cut to the diameter of the PMT tubes on opposite sides of the box. Two aluminum collars were also made to mount to these sides of the aluminum dark box and secure the PMTs with set screws. The walls of the dark box were then bolted together and electrical tape was triple wrapped along

all seams except for the seam along the lid of the box. The first PMT was set in place and locked down with set screws. The fiber bundle was placed on its stand inside the aluminum dark box and optically coupled to the first PMT. The second PMT was inserted into the box so that a small amount of compression pinched the fiber bundle between the two PMTs. Once compression was established, the second PMT was secured with set screws. Figure 21 shows what the fully constructed aluminum dark box looks like. Reusable putty was placed along the gap between the PMTs



**Figure 21.** Full view of the aluminum dark box used for data collection during the dual-ended readout portion of this investigation. The PMTs are secured to the box with set screw after pinching the fiber bundle inside the box. The box is designed with portability in mind, being placed in front of radiation sources that are not found in the laboratory.

and the aluminum collars to prevent light from getting inside the box. Putty was used because it could fill the gap and could also be easily moved whenever the PMT needed to be moved. See Figure 22 for what the putty looks like around the PMT tube. The lid was bolted down and triple-sealed with electrical tape after the fiber sample was secured and the radioactive source of interest was placed inside the box.



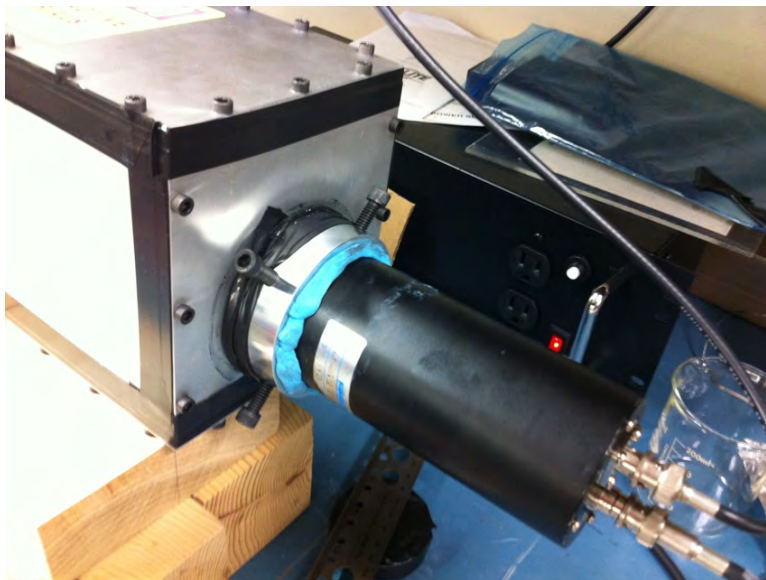


Figure 22. Close-up view of the PMT side of the aluminum dark box. Note the electrical tape wrapped around all seams of the box. Also worth noting is the blue putty wrapped around the PMT tube near the aluminum collar. The putty is squeezed between the gap formed by the aluminum collar and PMT tube. It was used because it is easy to pick up and move whenever the PMTs needed to be moved.

Three radioactive sources were used during this investigation: Cs-137 for gamma radiation, Am-241 for alpha radiation, and Sr-90 for beta radiation. Table 6 lists pertinent source information. The lone fiber, 2x1 bundle, and 7x3 bundle were

Table 6. Radioactive sources used during dual-ended readout portions of this research.

Isotope	Radiation	Energy [MeV]	Activity [ $\mu$ Ci]
Cs-137	Gamma	0.662	7.48
Am-241	Alpha	5.64	0.00019
Sr-90	Beta	0.546 (max)	0.074

separately irradiated with all three sources. Each source was placed at three different positions along the fiber bundle: 1 cm from the left end, the center of the bundle, and 1 cm from the right end of the bundle. All three sources were uncollimated and placed directly on the fiber. An additional experiment was performed using the Cs-

137 source. It was placed along the fibers in the same manner described previously, but the gammas were collimated using a lead block and the source was located 4 cm below the fiber bundle.

### 3.5 Exploration of CCD Capabilities

An investigation into the feasibility of using a commercial off-the-shelf (COTS) CCD camera to capture scintillation events coming from the fiber bundle was conducted. It is hoped that by combining timing information from the PMTs and position information from a CCD image of lit fibers, one can determine the path and energy of incident radiation through the bundle. The specifications of the camera used during this investigation can be found in Table 7.

**Table 7. Specifications of the CCD camera used during this investigation.**

Resolution	1024(H) x 768(V) Color or Mono
Pixel Pitch	4.65 $\mu\text{m}$ x 4.65 $\mu\text{m}$
Active Area	4.76 mm x 3.57 mm - 5.95 mm diagonal
Max Datarate	20 MHz
Responsivity	16.2 - 63.9 DN/(nJ/cm <sup>2</sup> )
Dynamic Range	59.7 dB
Bit Depth	8 and 12-bit
Exposure Range	63.5 $\mu\text{s}$ to 10 seconds
Gain	0 dB to 24.57 dB in 29 increments

Two experiments were designed to test the feasibility of imaging scintillation events with a CCD camera. Both experiments take place inside the large dark box seen in Figure 10. The setup for the first experiment uses a NaI crystal placed at the focal length of the CCD camera. Half of the NaI crystal was masked by electrical tape, leaving the other half bare. A Cs-137 radioactive source was placed directly on

top of the NaI crystal. The purpose of the mask is to create two distinct regions in the camera's field of view (FOV). One region should always be dark, while the other region can transmit the scintillation light to the camera. The location of the line separating these two regions is known beforehand so that comparisons can be made when images are taken of the scintillator in the dark. Figure 23 shows the setup for this experiment.



**Figure 23.** Experimental setup of NaI crystal imaging with the CCD camera inside the large dark box. The NaI crystal is placed at the focal length of the camera optics. Half of the crystal is covered with tape. The camera's FOV captures both the mask and the exposed crystal face. A Cs-137 source is placed on top of the crystal. Any scintillation light captured by the camera will only show up on the right side of image.

The second experiment places the front face of the 7x3 fiber bundle at the focal length of the CCD camera system. Again, the Cs-137 source was placed directly on top of the bundle. The location of each fiber in the bundle was imaged beforehand so that comparisons could be made when the scintillator images are taken in dark. Figure 24 shows the setup for this experiment.



Figure 24. Experimental setup of 7x3 fiber bundle imaging with the CCD camera inside the large dark box. The closest fiber bundle face to the camera is located at the focal length of the camera optics. A Cs-137 source is placed on top of the bundle, centered along the length of the fibers.

## IV. Analysis of Results

### 4.1 Simulation of Neutron Radiation on Fiber Bundles

The results of the MCNP simulations are presented in this section. A total of 42 simulations were run, split between 14 simulations for each of the four different source locations. The 14 simulations simulated 1x1, 2x2, 3x3, 4x4, 5x5, 6x6, 7x7, 8x8, 9x9, 10x10, 15x15, 20x20, 40x40, and 100x100 fiber bundles. Particle track information was saved for each simulation. The model was set up as described in Chapter III. These files were parsed using the MATLAB script located in Appendix E. The run time for processing these particle track files ranged from about 30 seconds for the 1x1 bundle simulations to over 5 hours for the 100x100 bundle simulations.

The energy deposition spectra for all fiber bundles simulated show the same basic features as seen in Figure 25. Note the full energy peak that begins to appear at 2.5 MeV from the 15x15 bundle onward, matching the incident neutron energy of 2.5 MeV. The peak occurring at around 0.70 MeV corresponds to collisions with carbon in the plastic scintillator. This matches with the theoretical maximum values of fractional energy transfer a neutron can transfer during elastic scattering as documented in Table 3 of Chapter II.

The results of the simulations where the source was located 5 cm from the left side of the bundle while staying centered longitudinally and vertically can be found in Figure 26. As can be seen in the figure, a gradient in energy deposition starts to be seen starting at the 10x10 fiber bundle onward. As the fiber bundle increases in size, so does the intrinsic efficiency as seen in Figure 27. A 40x40 bundle has  $6.7 \pm 0.2\%$  intrinsic efficiency for double scatter events.

The results of the simulations where the source was located 5 cm from the upper left corner of the bundle, while staying centered both longitudinally and vertically,

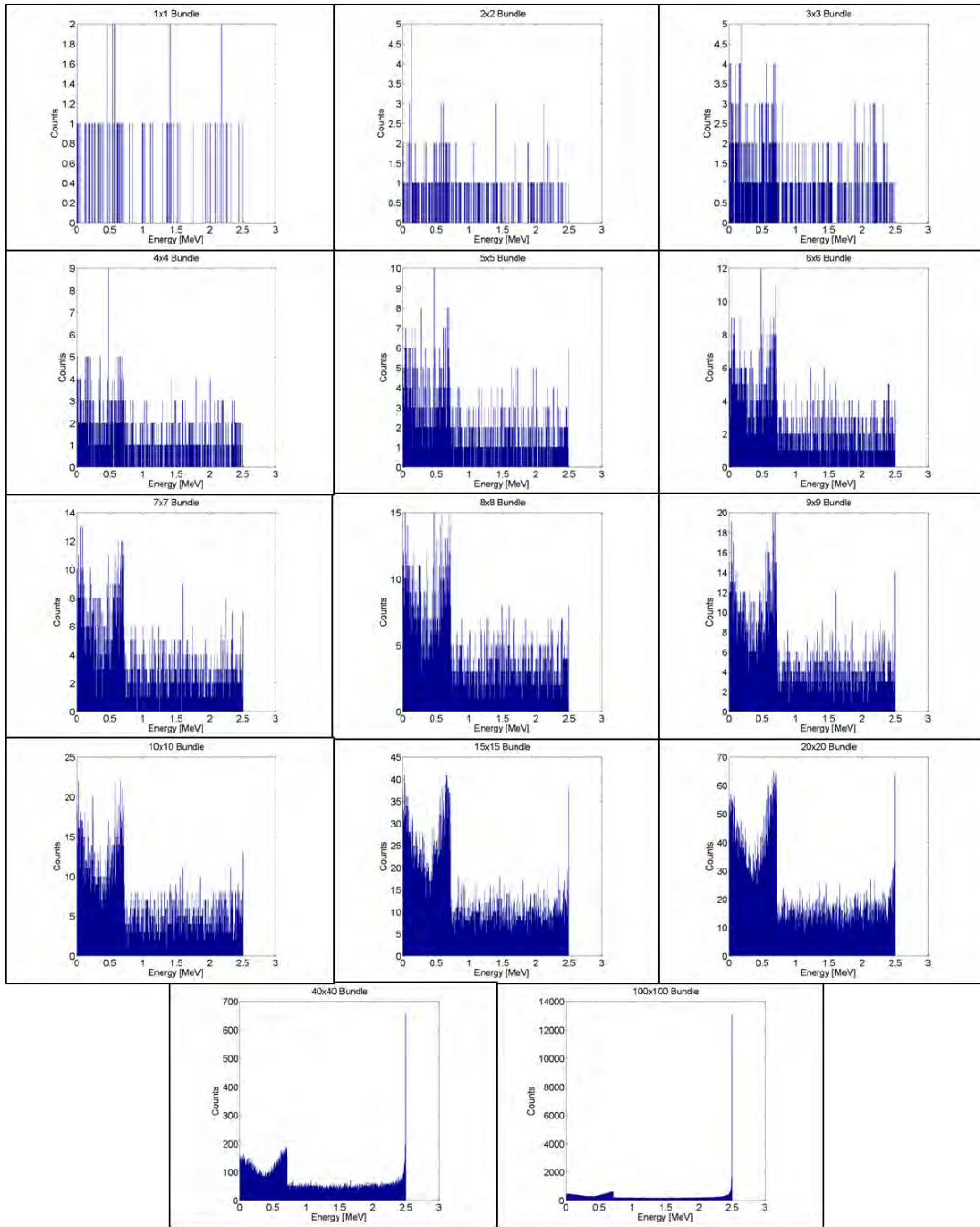


Figure 25. Progression of energy deposition spectra for 1x1, 2x2, 3x3, 4x4, 5x5, 6x6, 7x7, 8x8, 9x9, 10x10, 15x15, 20x20, 40x40, and 100x100 fiber bundles (left to right, top to bottom). The incident neutron energy is 2.5 MeV. Note the full energy peak that begins to appear at 2.5 MeV from the 15x15 bundle onward. Also worth noting is the peak occurring at around 0.70 MeV corresponding to collisions with carbon in the plastic scinillator. These features are common to all of the plots and become more apparent with larger bundle size.



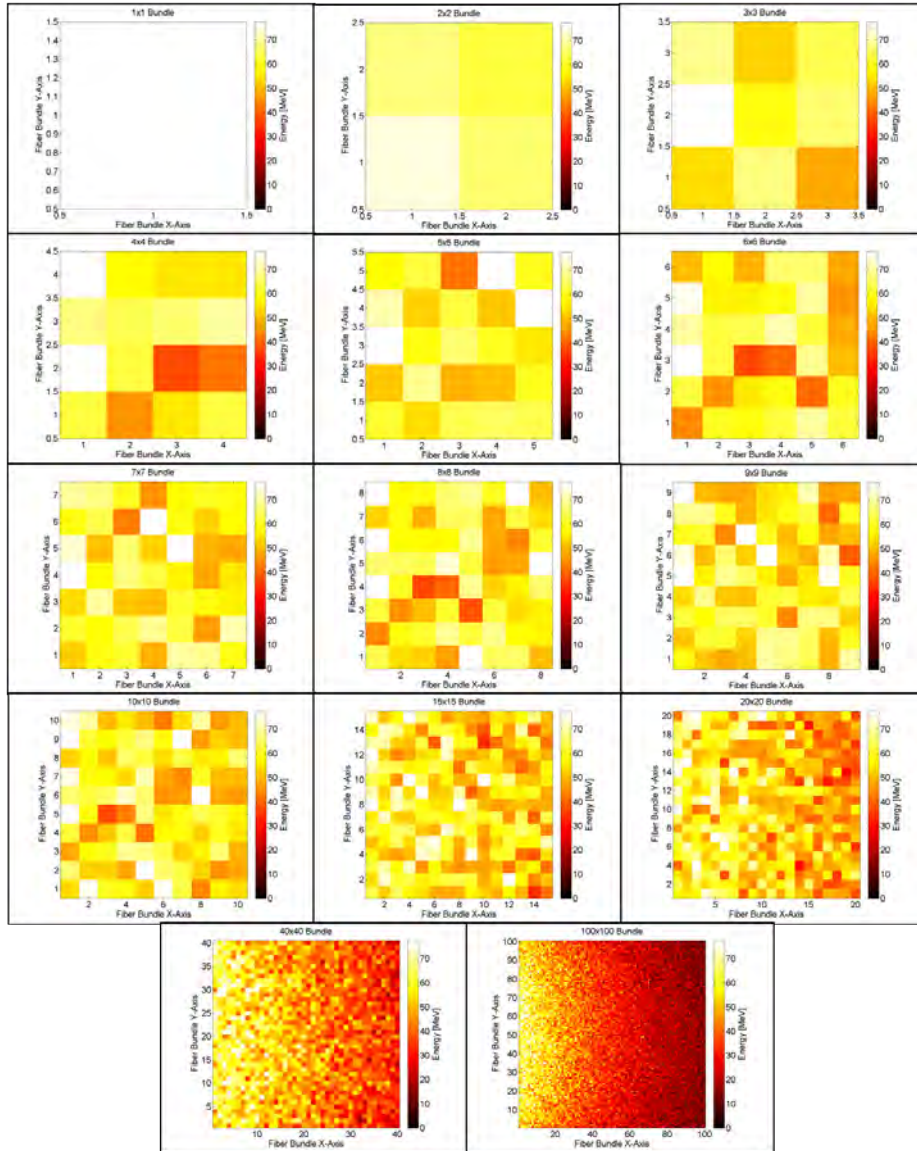
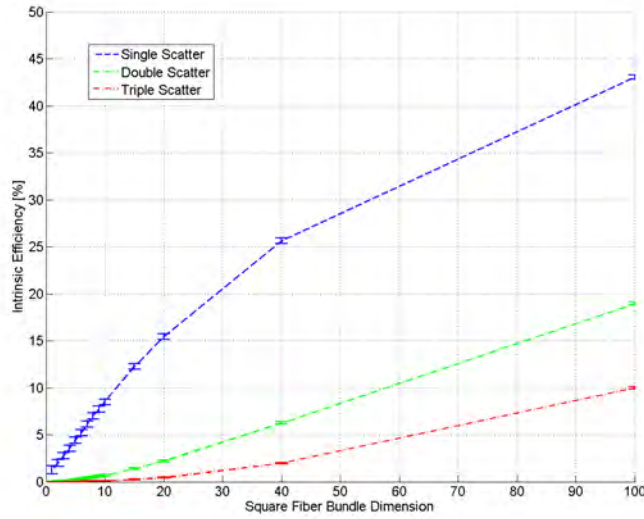


Figure 26. MCNP simulated energy deposited per fiber in a 1x1, 2x2, 3x3, 4x4, 5x5, 6x6, 7x7, 8x8, 9x9, 10x10, 15x15, 20x20, 40x40, and 100x100 fiber bundle (left to right, top to bottom). Lighter colors represent more energy deposited than darker colors. The location of the isotropic neutron source is defined by Part A of Figure 8. A noticeable gradient in energy deposition can be seen starting from the 15x15 bundle onward.



**Figure 27.** Intrinsic scattering efficiencies for single, double, and triple scatter events as a function of bundle size.

can be found in Figure 40. As seen previously, a gradient in energy deposition starts to be seen starting at the 10x10 fiber bundle onward. One can clearly observe the source position has changed between this group of simulations and the ones discussed earlier by the direction of this gradient. This energy deposited is again sufficient to produce measurable light output from each fiber.

The results of the simulations where the source was located 5 cm from the left side of the bundle while staying centered vertically, but located at the far end of the fiber bundle can be found in Figure 41 in Appendix A. Figure 42 in Appendix A has the same source parameters, except the source is at the near end of the fiber bundle instead of the far end.

An estimate of the time separation between double-scatter events was determined using the particle track results from 40x40 bundle with the source closest to the bundle. First, the distances between each double-scatter event were calculated. The distribution of these scatter events can be found in Figure [?]. The kinetic energy for each of these double-scatter neutrons during their transit from the first scatter site to



the second scatter site was also calculated. The distribution of neutron energies can be found in Figure [?]. Using non-relativistic kinematic equations, the distance from the first scatter site to the second scatter site, and neutron energy during transit, the time separation between double-scatter events was calculated. The distribution of double-scatter time separations can be found in Figure [?].

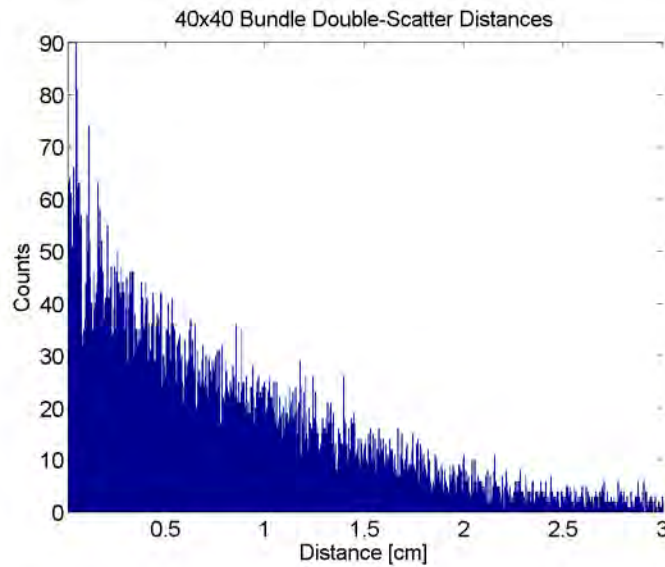


**Figure 28.** Distribution of scatter distances for double-scatter events in the 40x40 fiber bundle.

## 4.2 Characterizing PMT Dark Counts and Light Leakage

The results of characterizing the dark counts of the PMTs used during this investigation are presented in this section. Three methods at creating a dark environment around the PMTs were studied. These results of these methods are summarized in Table 9. As expected, the lowest dark count rate was achieved with the lens cap / aluminum can and collar system with a dark count rate of 15 per second. This setup is unrealistic for two reasons: there is no scintillator, hence no radiation detection

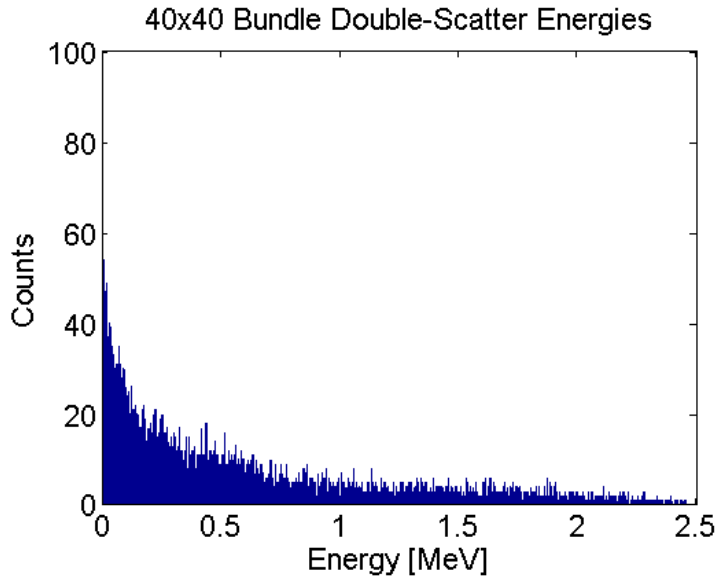


Figure 29. Distribution of transit energies for double-scatter events in the 40x40 fiber bundle.

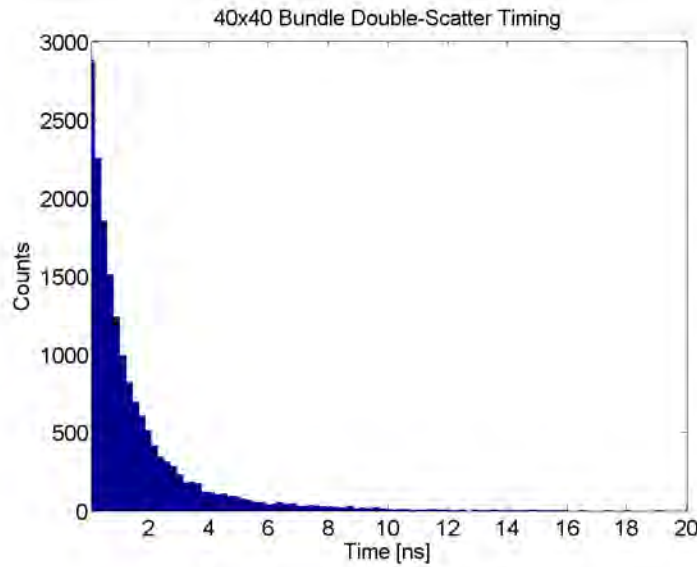


Figure 30. Distribution of scatter times for double-scatter events in the 40x40 fiber bundle. Over 40% of the double scatter events occur with a time separation of 1 ns or greater.

Table 8. Dark current and light leakage counts for the three dark configurations used in this investigation.

	Time to Million Counts [h]	Rate [Dark Counts/s]
Aluminum Can /w Lens Cap	18.7	15
Bare PMT in Large Dark Box	0.68	406
Aluminum Dark Box	1.2	229

can take place, and a cap completely covered the PMT window. The benefit of these results is they give a baseline of how many dark counts should be expected in an absolutely dark environment. The other two methods produced dark count rates that were 26x (for the PMT in the large dark box) and 16x greater (in the aluminum dark box). However, the setup of both of these experiments is representative of how data needs to be collected for dual-ended readout experiments.

Since a noisy environment is expected and the scintillation pulses may be as weak as dark count pulses, a method to distinguish between these two types of pulses is required. The experiment using the BC-404 bulk plastic scintillator addresses this. It is assumed that dark counts measured from a PMT arise from the dark current intrinsic to the PMT or from a few photons of stray light hitting the photocathode. As discussed in Chapter II, the light produced during scintillation is not produced instantaneously, but instead has a time-dependence. Therefore, a scintillation pulse should have a measurably wider width than a pulse caused by a dark event. An example of a dark count waveform can be found in Figure 31, while an example of a scintillation event waveform can be found in Figure 32.

Using the assumptions about voltage pulses from the output of a PMT discussed in Chapter II, an algorithm was written in MATLAB to calculate the decay constant for each waveform. A bimodal distribution of decay constants was discovered, illustrated in Figure 33. These two distributions are statistically different from each other using the standard  $3\sigma$  test as seen from the data presented in Table 9. The shorter decay constant distribution represents pulses arising from PMT dark current or light leakage. The longer decay constant distribution comes from scintillation events in the bulk plastic scintillator. Boundary values that delineate dark pulses from scintillation pulses can be determined, once the distribution of decay constants is known. A check

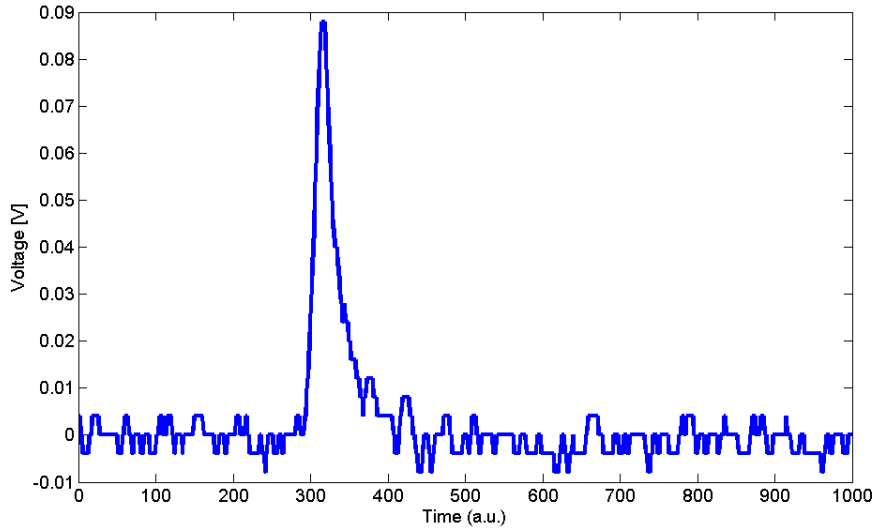


Figure 31. An example of a dark count waveform captured via a PMT made light-tight with the aluminum can and collar system seen in Figure 9.

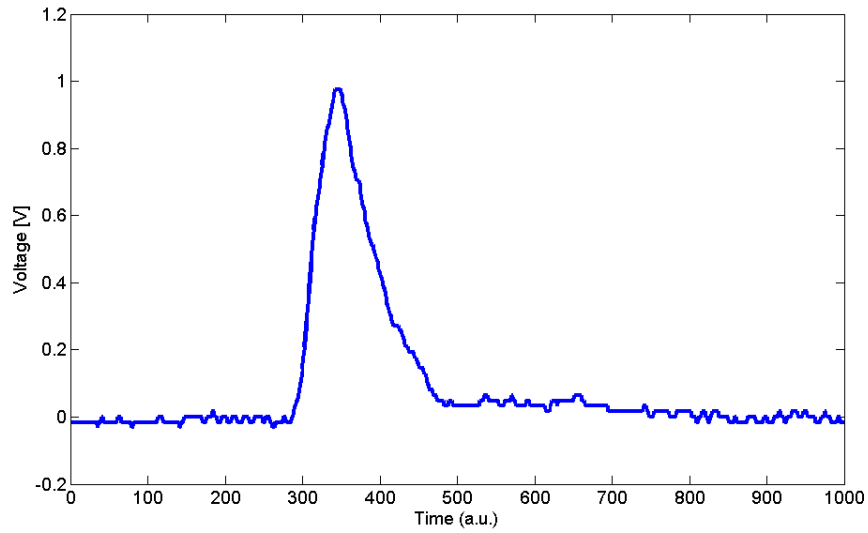
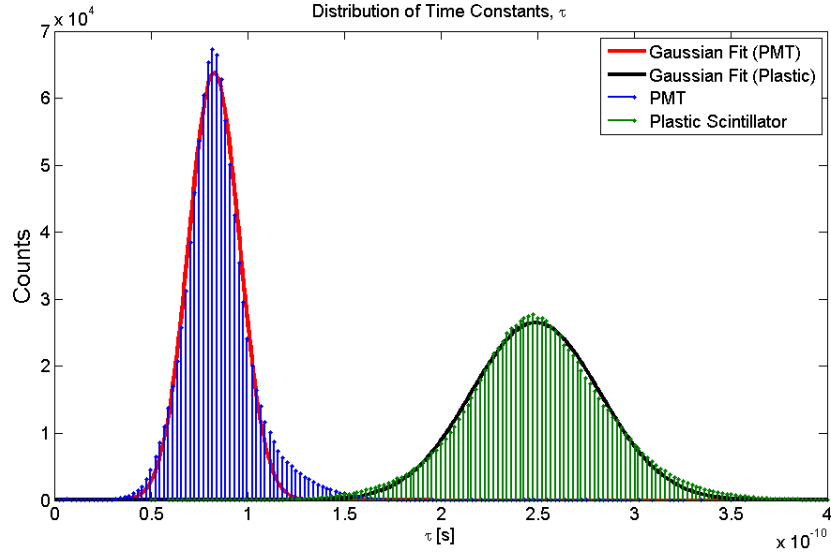


Figure 32. An example of a bulk plastic scintillation event waveform captured via a PMT made light-tight with the aluminum can and collar system seen in Figure 9.

Table 9. Dark current and light leakage counts for the three dark configurations used in this investigation.

	Time to Million Counts [h]	Rate [Dark Counts/s]
Aluminum Can /w Lens Cap	18.7	15
Bare PMT in Large Dark Box	0.68	406
Aluminum Dark Box	1.2	229



**Figure 33.** Comparison of the distribution of decay constants for PMT dark counts and bulk plastic scintillation events. The distributions are separated from each other by 3 standard deviations. Discrimination of noise events from scintillation events can be done at acquisition time using these distributions.

for these values can be inserted directly into the digital data acquisition code for real-time discrimination of dark events from scintillation events using a single PMT.

### 4.3 Dual-Ended Readout of Fibers

The results of the dual-ended readout experiments are presented in this section. As discussed in Chapter III, the two PMTs used in this investigation needed to be gain matched before any data was collected. Gain matching ensures that two PMTs will produce the same magnitude voltage pulse from the same amount of light collected. Slight differences in the materials and construction can cause a different response to the same high voltage bias for two different PMTs. The data plotted in Figure 34 uses the gain matching procedure outlined in Chapter III. By setting the two lines in those plots equal to each other, it was determined that if PMT A was set to 2.70 kV, then PMT B would need to be set to 2.74 kV to provide the same response as PMT A.

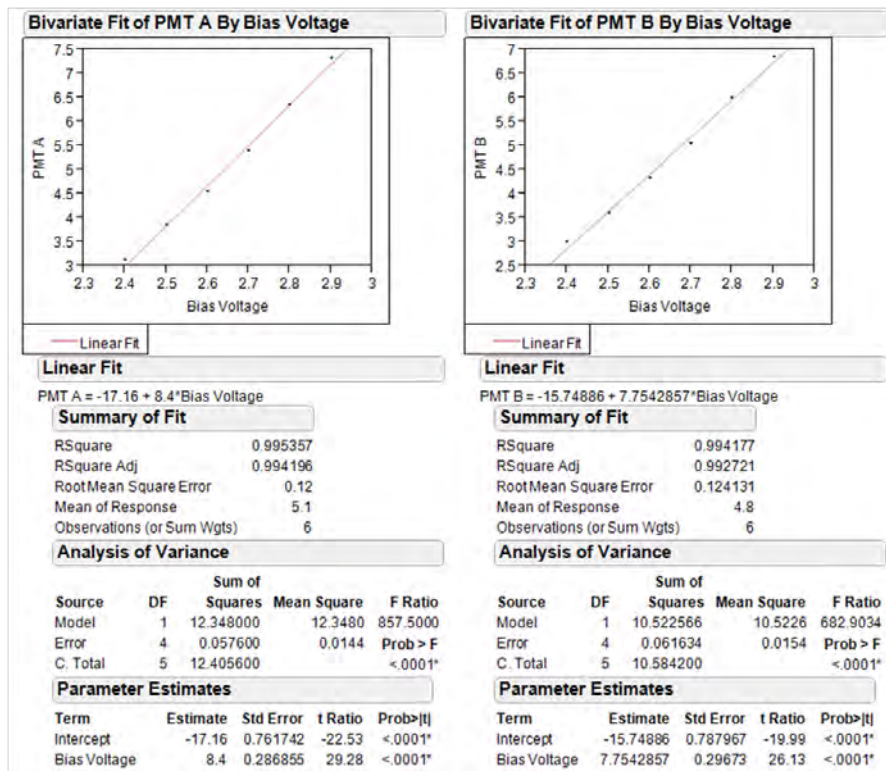
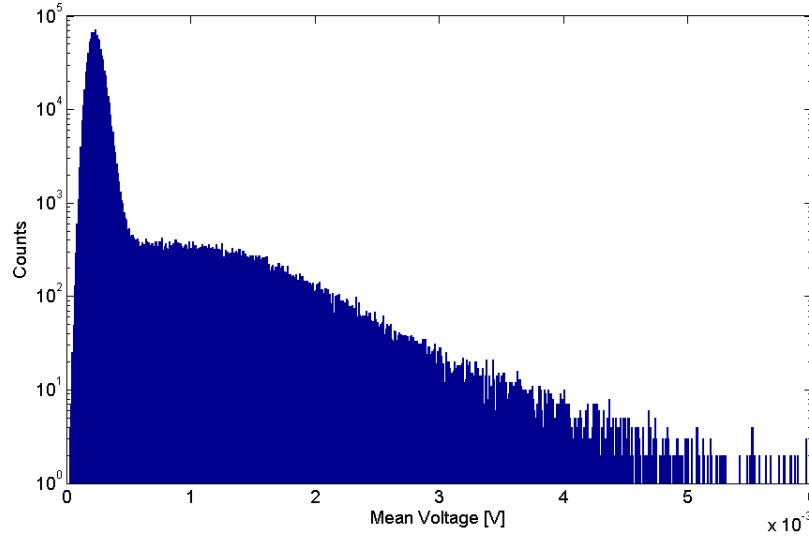


Figure 34. Linear regression analysis used to gain match the two PMTs used during this investigation. From this data it was determined that PMT A would be set to a bias of 2.70 kV, while PMT would be set to a bias of 2.74 kV. These bias settings ensured the response of either PMT would be the same for an identical scintillation light pulse.

Data from dual-ended readouts can be analyzed to discriminate out scintillator events from background noise. The raw mean voltage distributions without noise discrimination can be seen in Figure 35. It can be seen from that distribution that



**Figure 35.** Mean voltage distribution for an Am-241 source placed at the center of a single fiber. The distribution is actually comprised to two separate distributions. The peak at the far left shows contribution from noise events such as dark current pulses or light leakage events. The broader distribution to the right of that peak represents actual scintillation events.

the noise events would skew the mean value of the scintillation pulses toward lower voltages. Scintillation events are measured as pulses that occur within the same time window on both PMTs. Typically, non-scintillation events like dark current pulses or light leakage photons will only be measured on one PMT, but not on the other PMT within the same time window. An algorithm was developed to determine the distribution of mean voltages measured from PMT A whenever no pulse from PMT B rose 3 standard deviations above the noise floor. This algorithm determined that the noise events had a maximum mean voltage of 0.6 mV. This value was then discriminated out of the distributions of mean voltages for the single fiber and 7x3

fiber bundle irradiated by Cs-137, Am-241, and Sr-90. Table 10 lists the number of scintillation events, the mean voltage read from PMT A and the mean voltage read from PMT B for the single fiber irradiated by these sources. Table 11 lists the same

**Table 10. Mean voltage pulse values for scintillation events in a single BCF-12 scintillating fiber.**

Isotope	Scintillation Events	Ch 1 Mean Voltage [mV]	Ch 2 Mean Voltage [mV]
Cs-137	8,477	2.2	1.9
Am-241	29,697	1.4	1.2
Sr-90	15,520	1.4	1.2

information, except for the 7x3 bundle instead of the single fiber.

**Table 11. Mean voltage pulse values for scintillation events in a 7x3 bundle of BCF-12 scintillating fibers. Note the increase in mean voltages compared to the values in Table 10**

Isotope	Scintillation Events	Ch 1 Mean Voltage [mV]	Ch 2 Mean Voltage [mV]
Cs-137	271,181	2.2	1.9
Am-241	210,038	1.5	1.2
Sr-90	433,243	2.2	1.9

As expected, pulses measured from the 7x3 bundle are larger than those measured from the single fiber. This is because the interaction medium is larger in the fiber bundle; the light produced by multiple fibers should be greater than that produced by a single fiber. Discriminating out the noise events allows only the scintillation waveforms to be analyzed. A representative waveform measured from the single fiber irradiated with Sr-90 is seen in Figure 37. Compare this with to the 7x3 bundle irradiated with the same source, as seen in Figure ???. Notice the fiber bundle waveform is larger than the single fiber waveform. There are also more peaks seen in the fiber



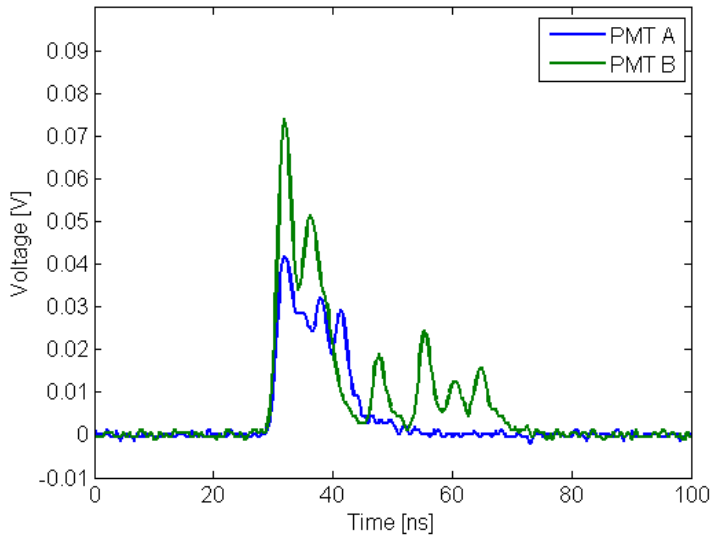


**Figure 36.** Representative waveform measured from the single fiber irradiated with Sr-90.

bundle waveforms compared to the single fiber. This could indicate that the PMT is fast enough to see individual fibers lighting up in the bundle. Representative waveforms for single fibers and fiber bundles irradiated with Am-241 and Cs-137 can be found in Appendix B.

The expected scintillation pulses measured from a PMT are characterized by a fast rise time followed by a slower exponential decay. However, the pulses measured from the single fibers and the fiber bundles show multiple peaks instead of a single decaying exponential. The timing separation between these peaks as well as the total number of peaks were studied. For the purposes of this analysis, a peak was defined as a local maxima that was at least  $6\sigma$  above the noise. The MATLAB code used to locate these peaks can be found in Appendix G. The distributions of time separation between the peaks of individual scintillation pulses for single fiber and a fiber bundle irradiated with Sr-90 can be found in Figure 38. The distributions of the number of peaks measured is found in Figure 39. If the multiple peaks were characteristic of a single fiber firing, then multiple scatter events in the fiber bundle should have

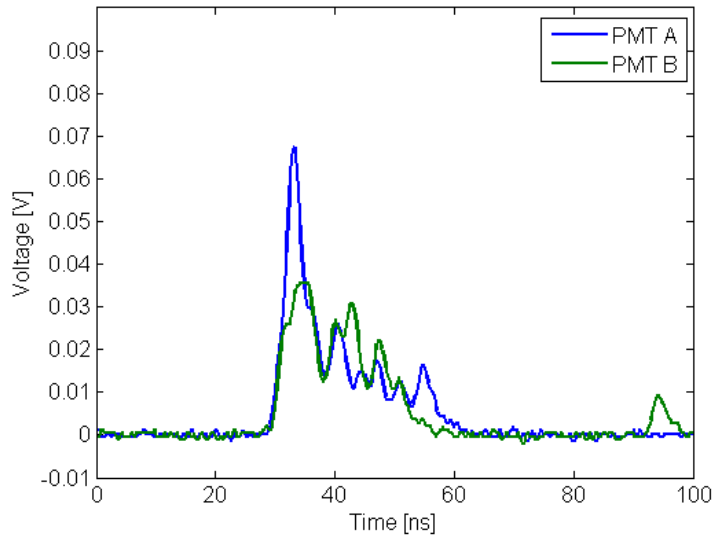


Figure 37. Representative waveform measured from the 7x3 fiber bundle irradiated with Sr-90.

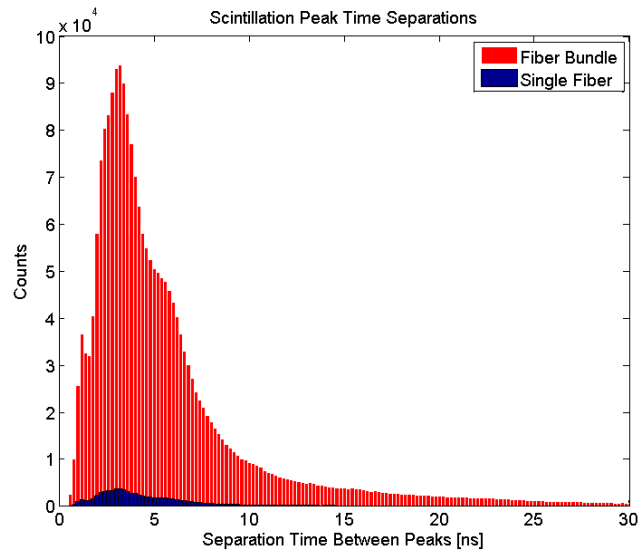
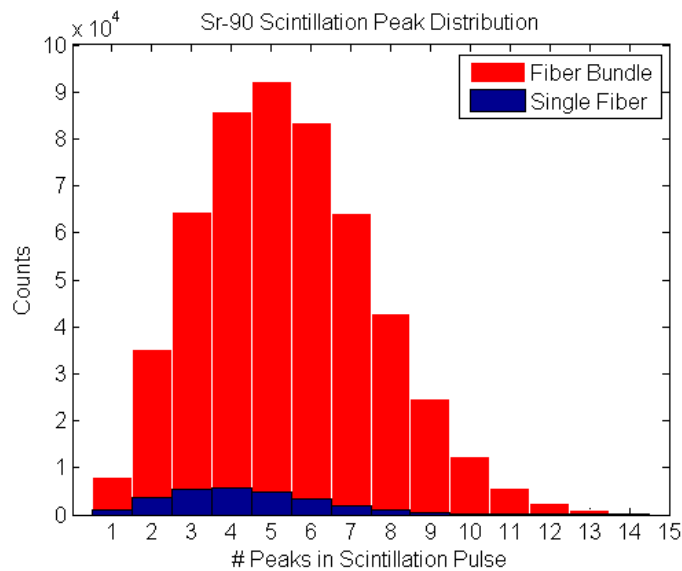


Figure 38. Distributions of peak separation times measured during Sr-90 irradiation of single fiber and 7x3 fiber bundle.



**Figure 39. Distributions of number of peaks measured during Sr-90 irradiation of single fiber and 7x3 fiber bundle.**

measurably more peaks. There was no statistically significant difference of the mean, median, or mode between the single fiber peaks and the fiber bundle peaks. This indicates no multiple scatter events were measured in the 7x3 fiber bundle irradiated with Sr-90. Similar results are seen when the fibers are irradiated with Cs-137 and Am-241 as seen in Appendix C.

## V. Conclusions

### 5.1 Conclusions

A MCNP transport model was developed with the objective of analyzing the interaction of neutrons with fiber bundles of varying size. A 2.5 MeV isotropic neutron source was modeled and placed at different locations relative to the fiber bundles. Five million source particles were simulated. A total of 42 simulations were run, split between 14 simulations for each of the four different source locations. A gradient in energy deposition starts to be seen starting at the 10x10 fiber bundles onward. A 40x40 bundle has  $6.7 \pm 0.2\%$  intrinsic efficiency for double scatter events. Over 40% of the double scatter events occur with a time separation of 1 ns or greater in the 40x40 bundle.

In order to measure only the pulses arising from a PMT's dark current, an absolutely dark environment needs to be created around the PMT's window. Three methods at creating a dark environment around the PMTs were studied. The lowest dark count rate was achieved with the lens cap / aluminum can and collar system with a dark count rate of 15 per second. The other two methods produced dark count rates that were 26x (for the PMT in the large dark box) and 16x greater (in the aluminum dark box). Since a noisy environment is expected and the scintillation pulses may be as weak as dark count pulses, a method to distinguish between these two types of pulses is required. A bimodal distribution of decay constants was discovered. These two distributions are statistically different from each other. Boundary values that delineate dark pulses from scintillation pulses can be determined, once the distribution of decay constants is known. A check for these values can be inserted directly into the digital data acquisition code for real-time discrimination of dark events from scintillation events using a single PMT.

Two kinds of fiber bundle were constructed for during this effort. The first fiber bundle was abandoned for three reasons. It was difficult to cleanly apply the epoxy, the method of cleaving the fiber left jagged fiber faces, and there was a slight bow over the length of the fiber bundle. The second type of fiber bundle created was a 7x3 array with no air gap between the fibers. This fiber bundle was inherently more rigid because of how the fibers are epoxied to each other, there is no bowing, and the fiber bundle faces are more reliably cleaved and polished when compared to the first fiber bundle type.

Measuring a scintillation light pulse simultaneously from both ends of a scintillating fiber can potentially be used to determine where the scintillation event took place along the length of the fiber. This kind of dual-ended readout is also useful in discriminating scintillation signals from a noisy background. Before any data collection using two PMTs took place, they were gain matched. Data from dual-ended readouts can be analyzed to discriminate out scintillator events from background noise. An algorithm was developed to determine the distribution of mean voltages measured from PMT A whenever no pulse from PMT B rose 3 standard deviations above the noise floor. As expected, pulses measured from the 7x3 bundle are larger than those measured from the single fiber. This is because the interaction medium is larger in the fiber bundle; the light produced by multiple fibers should be greater than that produced by a single fiber. No significant difference is measured between the multiple peaks seen in scintillation pulses of single fibers and fiber bundles. Multiple scatter events were not detected using a 7x3 fiber bundle. Construction of a 40x40 fiber bundle is recommended for future research due to its intrinsic efficiency and measurable double-scatter event probability.

## Appendix A. MCNP Particle Track Results

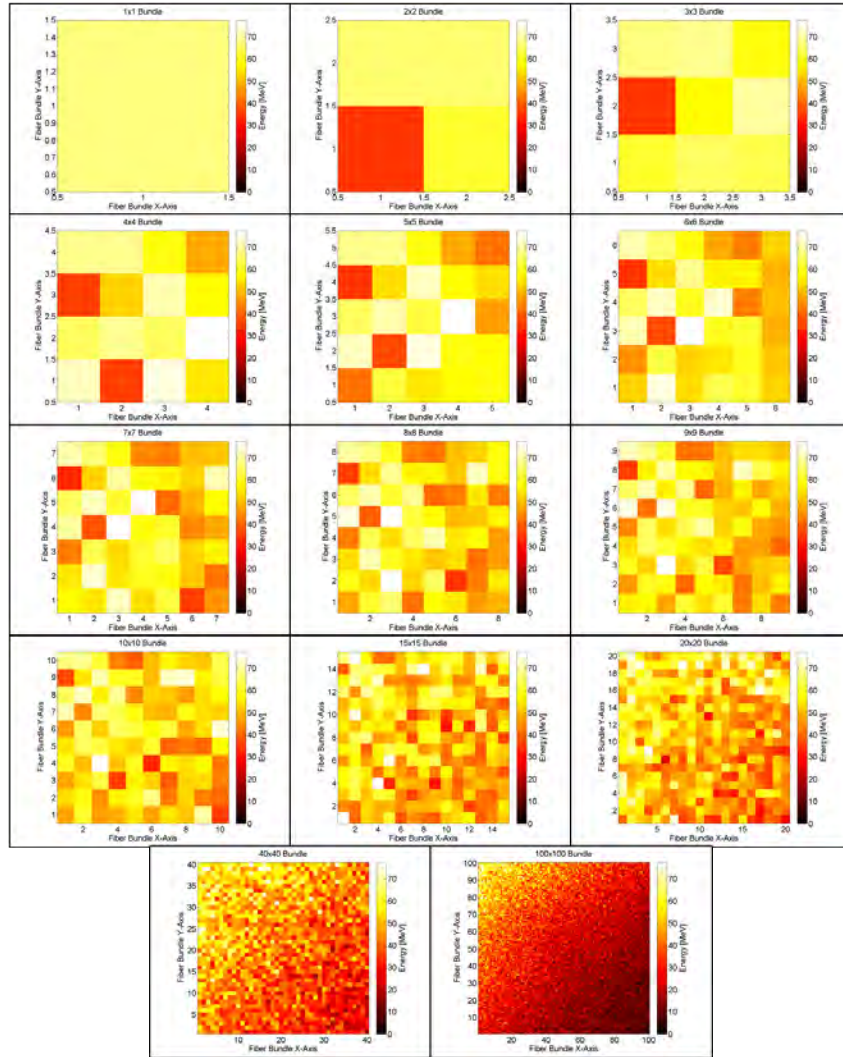


Figure 40. MCNP simulated energy deposited per fiber in a 1x1, 2x2, 3x3, 4x4, 5x5, 6x6, 7x7, 8x8, 9x9, 10x10, 15x15, 20x20, 40x40, and 100x100 fiber bundle (left to right, top to bottom). Lighter colors represent more energy deposited than darker colors. Note that the energy scale is identical to that of Figure 26. The location of the isotropic neutron source is defined by Part D of Figure 8. A noticeable gradient in energy deposition can be seen starting from the 15x15 bundle onward.

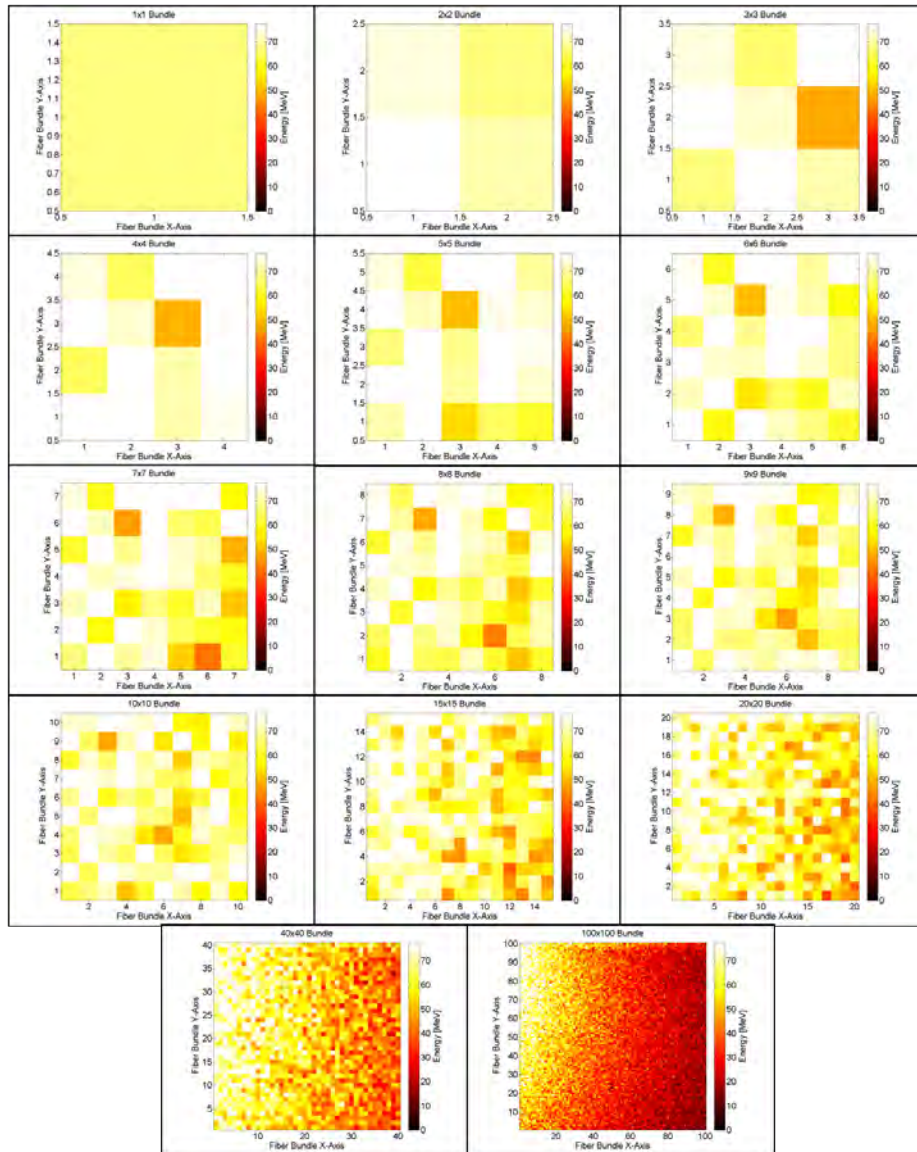


Figure 41. MCNP simulated energy deposited per fiber in a 1x1, 2x2, 3x3, 4x4, 5x5, 6x6, 7x7, 8x8, 9x9, 10x10, 15x15, 20x20, 40x40, and 100x100 fiber bundle (left to right, top to bottom). Lighter colors represent more energy deposited than darker colors. Note that the energy scale is identical to that of Figure 26. The location of the isotropic neutron source is defined by Part G of Figure 8. A noticeable gradient in energy deposition can be seen starting from the 20x20 bundle onward. Notice that more energy is deposited deeper inside the bundle compared to Figure 26.



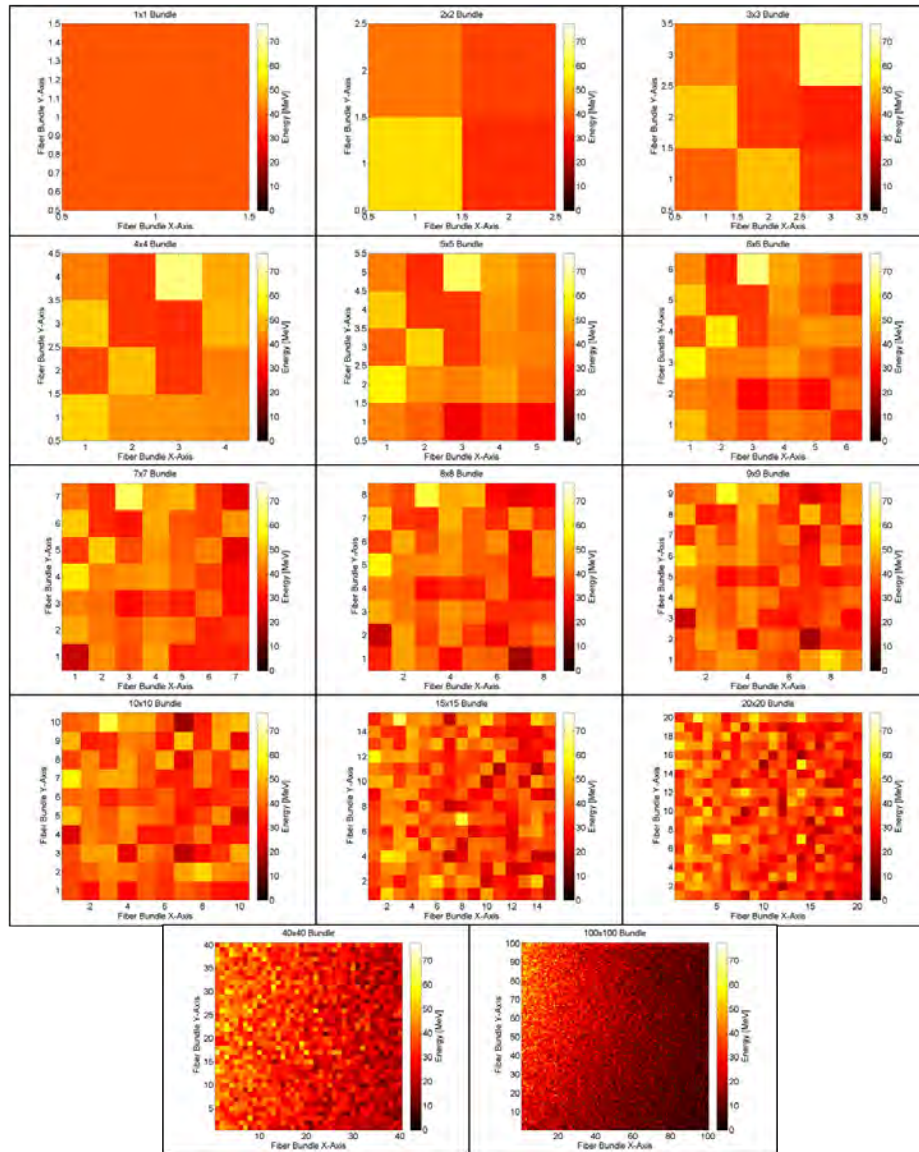


Figure 42. MCNP simulated energy deposited per fiber in a 1x1, 2x2, 3x3, 4x4, 5x5, 6x6, 7x7, 8x8, 9x9, 10x10, 15x15, 20x20, 40x40, and 100x100 fiber bundle (left to right, top to bottom). Lighter colors represent more energy deposited than darker colors. Note that the energy scale is identical to that of Figure 26. The location of the isotropic neutron source is defined by Part H of Figure 8. A noticeable gradient in energy deposition can be seen starting from the 40x40 bundle onward. Notice that less energy is deposited deeper inside the bundle compared to Figure 26.



## Appendix B. Representative Fiber Scintillation Pulses

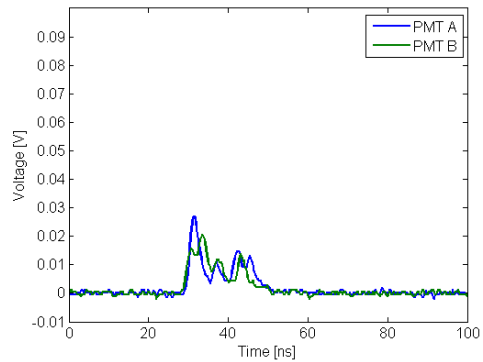


Figure 43. Representative waveform measured from the single fiber irradiated with Am-241.

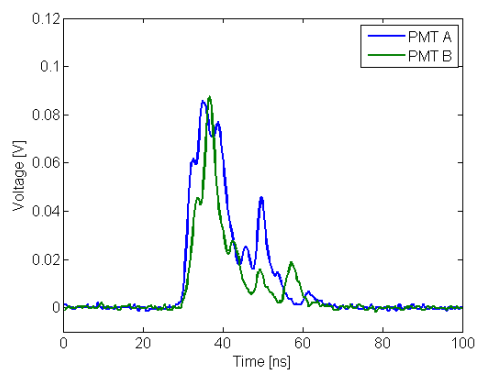


Figure 44. Representative waveform measured from the 7x3 fiber bundle irradiated with Am-241.

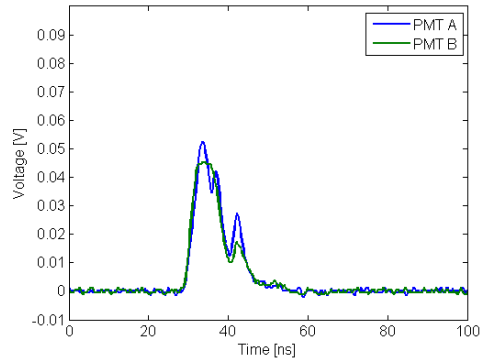


Figure 45. Representative waveform measured from the single fiber irradiated with Cs-137.

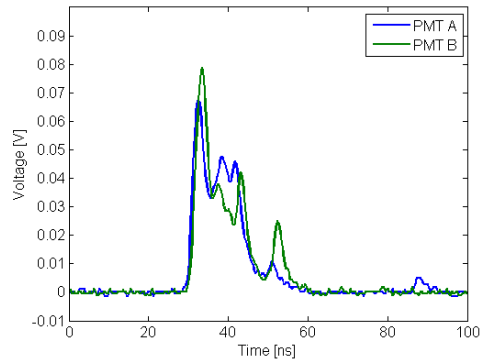


Figure 46. Representative waveform measured from the 7x3 fiber bundle irradiated with Cs-137.

## Appendix C. Scintillation Peak Distributions

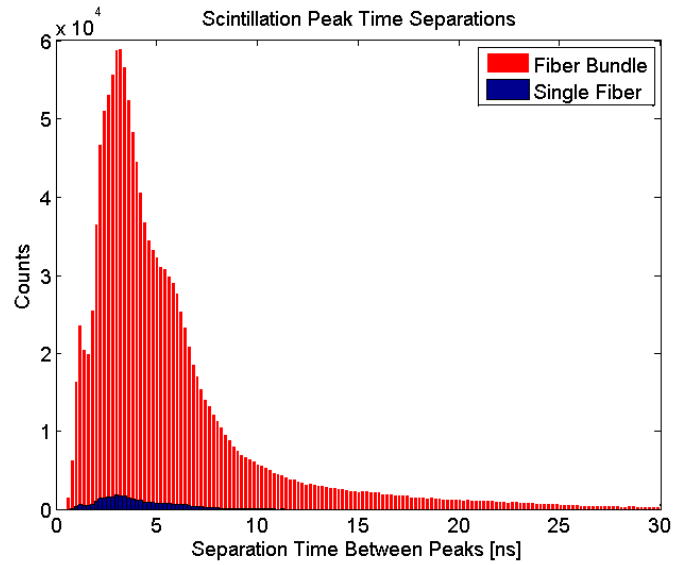


Figure 47. Distributions of peak separation times measured during Cs-137 irradiation of single fiber and 7x3 fiber bundle.

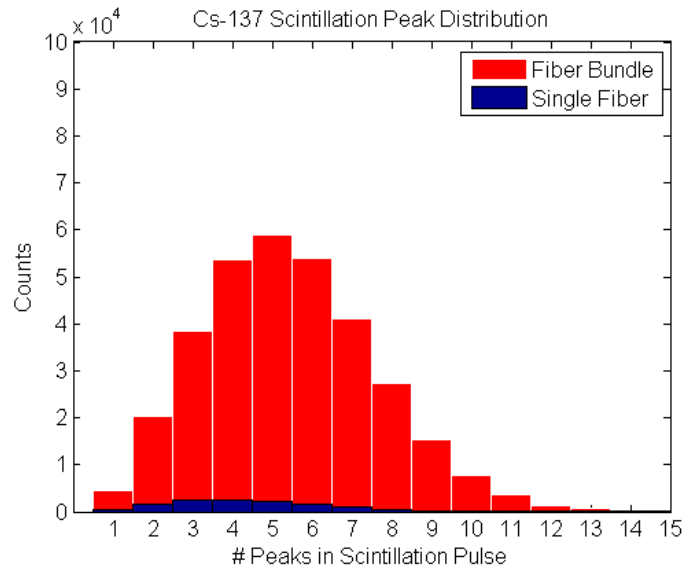


Figure 48. Distributions of number of peaks measured during Cs-137 irradiation of single fiber and 7x3 fiber bundle.

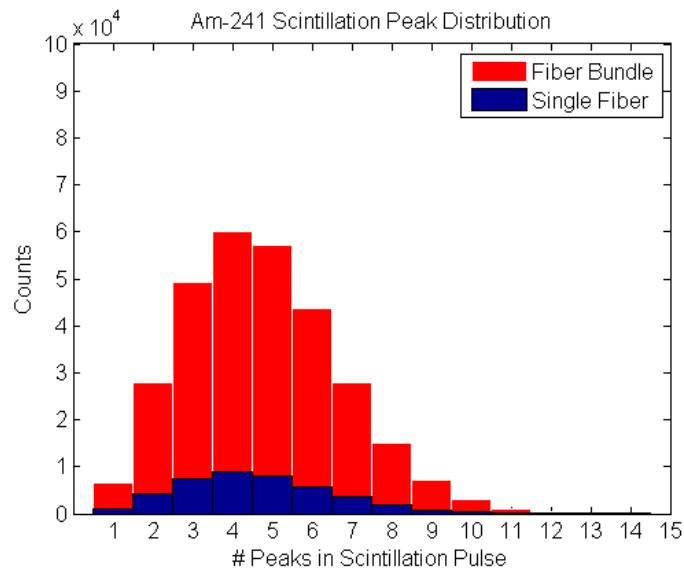


Figure 49. Distributions of number of peaks measured during Am-241 irradiation of single fiber and 7x3 fiber bundle.

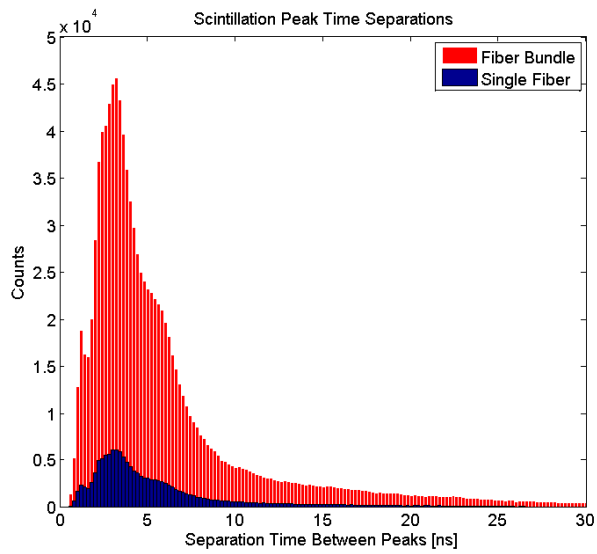


Figure 50. Distributions of peak separation times measured during Am-241 irradiation of single fiber and 7x3 fiber bundle.

## Appendix D. Dual Ended Readout Oscilloscope

```
1 %% Initialize Scope
  clc
  clear all
  close all

6 %%% Connection Variables
  visa_brand = 'tek'; % set to 'tek' for tektronix scopes
  visa_address = 'TCPIP::169.254.235.51::INSTR'; % use oscilloscope ...
    ip address
  buffer = 4000 * 1024; %2000 KiB

11 %%% Open Instrument
  fclose('all'); % close any open files - useful if this script was ...
    interrupted and you want to use it again
  dpo = visa(visa_brand, visa_address, 'InputBuffer', buffer, '...
    OutputBuffer', buffer); % create visa object, no instrument ...
    driver required!
  fopen(dpo); % open the instrument so that commands can be written ...
    to it

16 fwrite(dpo, '*RST'); % Reset scope to factory defaults - reset any ...
    inadvertant scope setting changes.
  fprintf('Scope reset to factory defaults.\n');
  %%% Configure Scope
  %%% Configuration Variables
  fprintf('Configuring scope....');

21 frames = 1000; % Number of waveforms to capture in FastFrame mode
  record = 1000; % Number of points in each individual waveform
  Ch1VPos = 4; % from -5.0 to 5.0 (the divisions on vertical axis)
  Ch1HPos = 15; % from 0 to 100 (divisions across the horizontal ...
    axis)
  Ch2VPos = 4; % from -5.0 to 5.0 (the divisions on vertical axis)
26 Ch2HPos = 30; % from 0 to 100 (divisions across the horizontal ...
    axis)
  Ch1Scale = 0.020; % [V]
  Ch2Scale = 0.020; % [V]
  Ch1Offset = 0.0; % [V]
  Ch2Offset = 0.0546; % [V]

31 TimeWindow = 5.0E-9; %width of time axis
  TimeStep = TimeWindow/record; % Returns seconds per point
  timearray = (1:1:record)*(TimeWindow/record)*1E9; % Array of time

  fwrite(dpo, 'ACQ:STATE 0'); % Turn off acquisition before we ...
    change scope settings
36 fwrite(dpo, 'HEAD 0'); % Turn off header information
  fwrite(dpo, 'ACQUIRE:MODE SAMPLE'); %Sets sampling mode to Sample ...
    mode
  fwrite(dpo, 'ACQUIRE:SAMPLINGMODE RT'); % Set Real Time sampling ...
    mode
```

```

fwrite(dpo,'HOR:MODE MANUAL'); % Enable manual adjustment of ...
    horizontal settings
fprintf(dpo,'HOR:MODE RECORD %i', record); % Set number of points ...
    on horizontal axis
41 fwrite(dpo,'HOR:FAST:STATE 1'); % Turn on FastFrame mode
fprintf(dpo,'HOR:FAST:COUNT %i', frames); % Set number of ...
    waveforms to capture per FastFrame acquisition
fprintf(dpo,'DATA:START 0'); % Sets the beginning of the ...
    individual waveform data to transfer (use 0)
fprintf(dpo,'DATA:STOP %i', record); % Sets the end of the ...
    individual waveform data to transfer
fwrite(dpo, 'DATA:ENCDG SRIBINARY'); % Set data encoding to least ...
    significant byte first, signed integer
46
fprintf(dpo,'WFMInpre:ENCDG BINARY'); % Sets incoming data to ...
    binary format
fprintf(dpo,'WFMInpre:BN_FMT RI'); % Set signed integer
fprintf(dpo,'WFMInpre:BYT_OR LSB'); %Transfer Least Significant ...
    Bit first
fprintf(dpo,'WFMInpre:BYT_NR 1');%Set 1 byte format = int8
51
fprintf(dpo,'WFMOupre:BYT_NR 1'); %Set 1 byte format = int16
fprintf(dpo,'WFMOupre:BN_FMT RI'); %Set signed integer
fprintf(dpo,'WFMOupre:BYT_OR LSB'); %Transfer Least Significant ...
    Bit first

56 fwrite(dpo,'Ch1:Termination 50') % Sets input impedance in Ohms (...
    use 50)
fwrite(dpo,'Ch2:Termination 50') % Sets input impedance in Ohms (...
    use 50)
fwrite(dpo,'Select:Ch1 On'); % Turns input for channel 1 on
fwrite(dpo,'Select:Ch2 On'); % Turns input for channel 2 on
fwrite(dpo,'DATA:SOURCE Ch1, Ch2'); % Sets data source to Channel ...
    1 and 2
61 fprintf(dpo,'Horizontal:Position %i', Ch1HPos); % Places signal at...
    designated horizontal location
fprintf(dpo,'ch1:Scale %i', Ch1Scale); % Sets vertical scale for ...
    channel 1
fprintf(dpo,'ch2:Scale %i', Ch2Scale); % Sets vertical scale for ...
    channel 2
fprintf(dpo,'CH1:Position %i', Ch1VPos); % Aligns channel 1
fprintf(dpo,'CH2:Position %i', Ch2VPos); % Aligns channel 2
66 fprintf(dpo,'Ch1:Offset %i', Ch1Offset); % Sets channel 1 offset
fprintf(dpo,'Ch2:Offset %i', Ch2Offset); % Sets channel 2 offset
fprintf(dpo,'Horizontal:Scale %i', TimeWindow); % Sets time scale
fprintf(dpo,'Horizontal:AcqLength %i', record); % Sets time ...
    resolution

71 query(dpo,'WFMOupre:YMult?');
Ch1YMult = str2double(query(dpo,'WFMOupre:YMult?')); % Returns ...
    vertical scale factor
Ch1Yoff = -Ch1VPos*Ch1Scale; % Calculate offset from zero

```

```

Ch2YMult = str2double(query(dpo,'WFMOutpre:YMult?')); % Returns ...
    vertical scale factor
Ch2Yoff = -Ch2VPos*Ch2Scale; % Calculate offset from zero
76 %%%%Edge Trigger Setting%%%%

fwrite(dpo,'Trigger:A:Type Edge'); % Edge mode trigger
fwrite(dpo,'Trigger:A:Edge:Slope Fall'); % Falling slope
81 fwrite(dpo,'Trigger:A:Level -0.010'); % Set trigger voltage level
fprintf(dpo,'Trigger:A:Mode Normal'); % Set trigger to Normal, ...
    apparently "Auto" is bad

%%%%%Pulse Width Trigger Setting%%%%%
86 %{
fwrite(dpo,'Trigger:A:Mode Normal'); % Set trigger to Normal, ...
    apparently "Auto" is bad
fwrite(dpo,'Trigger:A:Type Pulse'); % Pulse mode trigger
fwrite(dpo,'Trigger:A:Pulse:Class Width'); % Set to Pulse Width ...
    mode
fwrite(dpo,'Trigger:A:Pulse:Width:HighLimit 10.3E-9'); % Set upper...
    pulse limit [s]
91 fwrite(dpo,'Trigger:A:Pulse:Width:LowLimit 6.2E-9'); % Set lower ...
    pulse limit [s]
fwrite(dpo,'Trigger:A:Pulse:Width:Polarity Negative'); % Trigger ...
    off of negative polarity pulses
fwrite(dpo,'Trigger:A:Pulse:Width:When Within'); % Trigger when ...
    the time window occurs within the pulse
fwrite(dpo,'Trigger:A:Level -0.04'); % Set trigger voltage level;
%}
96

fprintf('Done!\n');

%% ACQUIRE DATA
101 sets = 1000; % How many datasets do you want to record?
tic % Start run time clock
Ch1 = zeros(1000,1000);
Ch2 = zeros(1000,1000);
for i=1:sets
106     fprintf(dpo,'Acquire:StopAfter Sequence'); % Stop acquiring ...
        after FastFrame acquisition
        fwrite(dpo,'ACQ:STATE 1'); % Turn on acquisition
        fprintf('Acquiring data set #%i.....', i);
        dpo.Timeout = 90; % Adjust MATLAB timeout so it is longer than...
            the acquisition duration
        query(dpo,'*opc?'); % Will return "1" when the acquisition is ...
            complete - used to sync curve command
111     dpo.Timeout = 10; % Decrease timeout time now that the ...
            acquisition is done
        fprintf('Done!\n');

```



```

fprintf(' Asking for waveforms....');
fwrite(dpo, 'curve?'); % Ask for waveforms - waveform preamble...
    and binary data will be stored in memory
116 fprintf('Done!\n');

fprintf(' Reading waveforms....');
fread(dpo,1); % Read and throw away first character in ...
    preamble - should be a "#"
bytes = str2double(char((fread(dpo,1)))); % Read and store the...
    number of bytes in memory
121 fread(dpo, bytes); % Read and throw away the appropriate ...
    number of characters remaining in the preamble
header = (1+1+bytes);
raw1 = fread(dpo, record*frames,'int8'); % Read and store all ...
    of the waveform data - no separation between individual ...
    waveforms
fread(dpo, header);
raw2 = fread(dpo, record*frames,'int8'); % Read and store all ...
    of the waveform data - no separation between individual ...
    waveforms
126 fprintf('Done!\n');
fread(dpo,1); % Read and throw away the termination character ...
    that Curve? adds

start = 1;
stop = 1000;
131 for j=1:frames
    Ch1(1:record, j) = raw1(start:stop);
    Ch2(1:record, j) = raw2(start:stop);
    start = stop+1;
    stop = start+record-1;
136 end

Ch1 = -(Ch1YMult*Ch1+Ch1Yoff); % Apply scale and offset to ...
    match the physical voltage values
Ch2 = -(Ch2YMult*Ch2+Ch2Yoff); % Apply scale and offset to ...
    match the physical voltage values
savename = ['Ch1_' num2str(i) '.mat']; % name the current ...
    batch of waveforms
141 save(savename,'Ch1') % save the current batch of waveforms
savename = ['Ch2_' num2str(i) '.mat']; % name the current ...
    batch of waveforms
save(savename,'Ch2') % save the current batch of waveforms
end
fprintf('***** %i waveforms recorded! *****\n', sets*...
frames*2);
146 timeElapsed = toc % End run time clock

```

## Appendix E. Particle Track Code

```
%{
2 MCNP5 Fiber Bundle Particle Track Parser
  Given a set of particle track files with the filename structure ...
  given
  by: #x#_@.ptr, where # is the x and y dimensions (respectively of ...
  the fiber
  bundle and @ is a character corresponding to the data set being ...
  processed
%}
7 close all
  clear all
  clc

% this array corresponds to the name of the mcnp ptrac files being
12 % processed
dim = [1,2,3,4,5,6,7,8,9,10,15,20,40,100];
data_sets = ['a', 'b', 'c', 'd', 'e', 'f', 'g', 'h'];

for r = 1:length(data_sets)
17   set = data_sets(r); % data set being processed (the "@" in the...
      introduction)
  for q = 1:length(dim) % loop through all files
    fprintf('Processing: %ix%i_%c.ptr\n', dim(q), dim(q), set);
    nscatter = zeros(1,100);
    int_list = [];
22   energy = [];
    tic; % start run time clock
    % open file
    fid = fopen([set '/' num2str(dim(q)) 'x' num2str(dim(q)) '_' ...
                set '.ptr']);
    for i=1:10
27       fgetl(fid); %skip first 10 lines
    end
    line = 1; % current line number being looked at, starts after ...
            header
    k = 1; % index used to keep track of energy deposited
    m = 1; % index used to keep track of interaction events
32   hits = 0; % number of histories that occur within bundle
    %{
    The while loop reads from the file one line at a time until it
    reaches the end of the file. It continuously builds up the
    variable called "data" which is just a list of the individual ...
    lines
37   read in. When it encounters a "9000" in the first column it ...
      reads
    the next line and stops to perform some calculations. 9000
    corresponds to a terminal event in the particle track. The ...
    calculations
    at this point create the interaction list and track the hits
    %}
```

```

42 while(~feof(fid)) % read from file until you reach the end of ...
    the file
    s = fgetl(fid); % read a line from the file
    char_line = sscanf(s(:), '%c'); % read all characters ...
        in line
    data(line,1:length(char_line)) = char_line; % buildup list...
        of lines
47 if (strcmp(data(line,7:11), ' 9000') == 1)
    s = fgetl(fid); % read another line from the file
    char_line = sscanf(s(:), '%c'); % read all characters ...
        in line
    data(line+1,1:length(char_line)) = char_line; %read ...
        last line
    hits = hits+1; % increment hits
    data_size = size(data); % calculate dimensions of data...
        variable
52 data_rows = data_size(1); % pull out # rows from size ...
        variable
    %{
    the for loop cycles through the current data block ...
        until it
    finds a 4000, corresponding to a collision event, it ...
        then
    record the cell number, energy deposited and the atom ...
        the
57 collision took place with into the interaction list
    %}
    for i=1:data_rows
        if strcmp(data(i,7:11), ' 4000') == 1
            int_list(m, 1) = str2double(data(i,46:51));
62             int_list(m, 2) = str2double(data(i+2,28:32));
            int_list(m, 3) = str2double(data(i+1,81:93)) ...
                ...
                - str2double(data(i+3,81:93));
            int_list(m, 4) = m;
            m = m+1;
67         end
    end
    p_energy = str2double(data(data_rows,81:93));
    collision = str2double(data(data_rows-1,69:71));
    if isnan(collision) == 0
72         if (collision ~= 0)
            nscatter(collision) = nscatter(collision)+1;
        end
    end
    if (p_energy ~= 2.5)
77         energy(k) = 2.5 - p_energy;
            k = k+1;
        end
    clear data;
    line = 1;
82 end

```

```
        line = line + 1;
    end
    save([set '/' num2str(dim(q)) 'x' num2str(dim(q)) '_' set '....
        mat'], ...
        'int_list', 'energy', 'nscatter', 'hits')
87   toc
    end
end
```

## Appendix F. MCNP Input File Generation Code

```
1 close all
  clear all
  clc
  dim = [1,2,3,4,5,6,7,8,9,10,15,20,40,100];
  set = 'g';
6 for q =1:length(dim)
  tic;
  number_fibers_x = dim(q); % number of fibers in the x-direction
  number_fibers_y = dim(q); % number of fibers in the y-direction
  fiber_diameter = 0.0500; % fiber diameter [cm]
11 fiber_length = 19.0*0.5; % fiber length in the z-direction [cm]
  total_fibers = number_fibers_x*number_fibers_y; % total number of ...
    fibers in the bundle
  spacing = fiber_diameter*1.01; % cells that hold fibers are %1 ...
    bigger than the fibers themselves

  world_diameter = 200; % diameter of world sphere [cm]
16 world_id = total_fibers+number_fibers_x+number_fibers_y+2+3; % ...
    surface id for world sphere
  fiber_start_id = total_fibers+number_fibers_x+number_fibers_y+2+1;...
    % id of start plane for fibers
  fiber_end_id = fiber_start_id+1; % id of end plane for fibers

  source_pos = [-5, number_fibers_y*fiber_diameter+0.5, fiber_length...
    *0.5]; % xyz position of source, fiber bundle is in first ...
    quadrant, positive z
21 number_of_particles = 5000000; % number of particles to run

  x_planes = zeros(number_fibers_x+1,1); % planes that form borders ...
    between fiber cells in x-direction
  y_planes = zeros(number_fibers_y+1,1); % planes that form borders ...
    between fiber cells in y-direction

26 x_planes(1) = -spacing/2; % first border plane in x-direction
  for k=2:number_fibers_x+1
    x_planes(k) = x_planes(k-1)+spacing;
  end
  y_planes(1) = -spacing/2; % first border plane in x-direction
31 for k=2:number_fibers_y+1
    y_planes(k) = y_planes(k-1)+spacing;
  end

  fid = fopen([num2str(number_fibers_x) 'x' num2str(number_fibers_y)...
    '_' set '.in'], 'w'); % open file for writing
36 fprintf(fid, 'fiber array test\n'); % title
  for i=1:total_fibers % write fiber cells
    fprintf(fid, '%i 1 -1.05 -%i %i -%i imp:n=1\n', i, i, ...
      fiber_start_id, fiber_end_id);
  end
end
```

```

41 n = total_fibers+1; % current cell index after writing fiber cells
for i=1+number_fibers_y+total_fibers:number_fibers_y+...
    number_fibers_x+total_fibers
    for j=1+total_fibers:number_fibers_x+total_fibers
        fprintf(fid, '%i 0 %i %i -%i %i -%i %i -%i imp:n=1\n', n, ...
            n-total_fibers, j, j+1, i+1, i+2, fiber_start_id, ...
            fiber_end_id); % fiber cells
        n = n+1; % increment cell index
46     end
end

fprintf(fid, '%i 0 #(%i -%i %i -%i %i -%i) -%i imp:n=1\n',n, 1+...
    total_fibers, total_fibers+number_fibers_x+1, total_fibers+...
    number_fibers_x+2, 2+number_fibers_y+number_fibers_x+...
    total_fibers, fiber_start_id, fiber_end_id, world_id); % cell ...
    that holds bundle
51 fprintf(fid, '%i 0 %i imp:n = 0\n', n+1, world_id); % world cell

fprintf(fid, '\n');
fprintf(fid, 'c === Surface Cards ...
===== \n');
n = 1;
56 for y=0:spacing:(number_fibers_y-1)*spacing
    for x=0:spacing:(number_fibers_x-1)*spacing
        fprintf(fid, '%i c/z %f %f %f\n', n, x, y,(fiber_diameter...
            /2));
        n = n+1;
    end
61 end

for i=1:length(x_planes)
    fprintf(fid, '%i px %f\n', n, x_planes(i));
    n = n+1;
66 end
for i=1:length(y_planes)
    fprintf(fid, '%i py %f\n', n, y_planes(i));
    n = n+1;
end
71
fprintf(fid, '%i pz 0\n', fiber_start_id); %end cap
fprintf(fid, '%i pz %f\n', fiber_end_id, fiber_length); %end cap
fprintf(fid, '%i so %f\n', world_id, world_diameter/2); % world ...
    sphere
fprintf(fid, '\n');
76 fprintf(fid, 'c === Materials ...
===== \n')...
;
fprintf(fid, 'm1      1001 0.50 6012 0.50\n');
fprintf(fid, 'c ===== Source ...
===== \n')...
;

```

```

fprintf(fid, 'sdef erg=2.5 par=1 pos = %f %f %f\n', source_pos(1),...
    source_pos(2), source_pos(3));
fprintf(fid, 'c ===== Histories ...
===== \n');
81 fprintf(fid, 'nps %f\n', number_of_particles);
fprintf(fid, 'c ===== Cutoffs, physics, and variance reduction...
===== \n');
fprintf(fid, 'mode n\n');
fprintf(fid, 'ptrac write=all file=asc max=%f &\n', ...
    number_of_particles*20);
fprintf(fid, '          filter=1,%i,icl\n',total_fibers);
86 % fprintf(fid, '          cell=');
% for i=1:total_fibers-1
%     if (mod(i,10) ~=0)
%         fprintf(fid, '%i,', i);
%     else
91 %         fprintf(fid, ' &\n          %i,', i);
%     end
% end
% fprintf(fid, '%i\n',total_fibers);

96 fclose all;

toc
end

```

## Appendix G. Find Maxima Code

```
1 function [xmax,imax,xmin,imin] = extrema(x)
%EXTREMA Gets the global extrema points from a time series.
% [XMAX,IMAX,XMIN,IMIN] = EXTREMA(X) returns the global minima ...
and maxima
% points of the vector X ignoring NaN's, where
% XMAX - maxima points in descending order
6 % IMAX - indexes of the XMAX
% XMIN - minima points in descending order
% IMIN - indexes of the XMIN
%
% DEFINITION (from http://en.wikipedia.org/wiki/...
Maxima_and_minima):
11 % In mathematics, maxima and minima, also known as extrema, are ...
points in
% the domain of a function at which the function takes a largest...
value
% (maximum) or smallest value (minimum), either within a given
% neighbourhood (local extrema) or on the function domain in its...
entirety
% (global extrema).
16 %
% Example:
% x = 2*pi*linspace(-1,1);
% y = cos(x) - 0.5 + 0.5*rand(size(x)); y(40:45) = 1.85; y...
(50:53)=NaN;
% [ymax,imax,ymin,imin] = extrema(y);
21 % plot(x,y,x(imax),ymax,'g.',x(imin),ymin,'r.')
```

%

% See also EXTREMA2, MAX, MIN

%

% Written by

26 % Lic. on Physics Carlos Adrin Vargas Aguilera

% Physical Oceanography MS candidate

% UNIVERSIDAD DE GUADALAJARA

% Mexico, 2004

%

31 % nubeobscura@hotmail.com

%

% From : <http://www.mathworks.com/matlabcentral/fileexchange>

% File ID : 12275

% Submitted at: 2006-09-14

36 % 2006-11-11 : English translation from spanish.

% 2006-11-17 : Accept NaN's.

% 2007-04-09 : Change name to MAXIMA, and definition added.

%

```
41 xmax = [];
imax = [];
xmin = [];
imin = [];
```



```

46 % Vector input?
    Nt = numel(x);
    if Nt ~= length(x)
        error('Entry must be a vector.')
    end
51
    % NaN's:
    inan = find(isnan(x));
    indx = 1:Nt;
    if ~isempty(inan)
56     indx(inan) = [];
        x(inan) = [];
        Nt = length(x);
    end

61 % Difference between subsequent elements:
    dx = diff(x);

    % Is an horizontal line?
    if ~any(dx)
66     return
    end

    % Flat peaks? Put the middle element:
    a = find(dx~=0);           % Indexes where x changes
71 lm = find(diff(a)~=1) + 1; % Indexes where a do not changes
    d = a(lm) - a(lm-1);      % Number of elements in the flat ...
        peak
    a(lm) = a(lm) - floor(d/2); % Save middle elements
    a(end+1) = Nt;

76 % Peaks?
    xa = x(a);                % Serie without flat peaks
    b = (diff(xa) > 0);        % 1 => positive slopes (minima begin)
                                % 0 => negative slopes (maxima begin)
    xb = diff(b);             % -1 => maxima indexes (but one)
81                                % +1 => minima indexes (but one)
    imax = find(xb == -1) + 1; % maxima indexes
    imin = find(xb == +1) + 1; % minima indexes
    imax = a(imax);
    imin = a(imin);

86
    nmaxi = length(imax);
    nmini = length(imin);

    % Maximum or minumim on a flat peak at the ends?
91 if (nmaxi==0) && (nmini==0)
        if x(1) > x(Nt)
            xmax = x(1);
            imax = indx(1);
            xmin = x(Nt);

```

```

96   imin = indx(Nt);
    elseif x(1) < x(Nt)
        xmax = x(Nt);
        imax = indx(Nt);
        xmin = x(1);
101  imin = indx(1);
    end
    return
end

106 % Maximum or minumim at the ends?
    if (nmaxi==0)
        imax(1:2) = [1 Nt];
    elseif (nmini==0)
        imin(1:2) = [1 Nt];
111 else
        if imax(1) < imin(1)
            imin(2:nmini+1) = imin;
            imin(1) = 1;
        else
116   imax(2:nmaxi+1) = imax;
            imax(1) = 1;
        end
        if imax(end) > imin(end)
            imin(end+1) = Nt;
121 else
            imax(end+1) = Nt;
        end
    end
    xmax = x(imax);
126 xmin = x(imin);

    % NaN's:
    if ~isempty(inan)
        imax = indx(imax);
131 imin = indx(imin);
    end

    % Same size as x:
    imax = reshape(imax,size(xmax));
136 imin = reshape(imin,size(xmin));

    % Descending order:
    [temp,inmax] = sort(-xmax); clear temp
    xmax = xmax(inmax);
141 imax = imax(inmax);
    [xmin,inmin] = sort(xmin);
    imin = imin(inmin);

146 % Carlos Adrin Vargas Aguilera. nubeobscura@hotmail.com

```

## Bibliography

- [1] Abdi, O., K.C. Wong, T. Hassan, K.J. Peters, and M.J. Kowalsky. “Cleaving of solid single mode polymer optical fiber for strain sensor applications”. *Optics Communications*, 282(5):856 – 861, 2009. ISSN 0030-4018. URL <http://www.sciencedirect.com/science/article/pii/S0030401808011218>.
- [2] Achenbach, P., C. Ayerbe Gayoso, J. Bernauer, R. Bhm, M.O. Distler, L. Doria, J. Friedrich, H. Merkel, U. Mller, L. Nungesser, J. Pochodzalla, S. Snchez Majos, S. Schlimme, Th. Walcher, and M. Weinriefer. “Measurement of propagation time dispersion in a scintillator”. *Nuclear Instruments and Methods in Physics Research Section A: Accelerators, Spectrometers, Detectors and Associated Equipment*, 578(1):253 – 260, 2007. ISSN 0168-9002. URL <http://www.sciencedirect.com/science/article/pii/S0168900207010236>.
- [3] Birks, J. B. *The Theory and Practice of Scintillation Counting*. Pergamon Press, Ltd., 1964.
- [4] Brannon, E. and G.L. Olde. *Radiation Research*, 16:1, 1962.
- [5] Chadwick, J. “The Existence of a Neutron”. *Royal Society of London Proceedings Series A*, 136:692–708, June 1932.
- [6] Craun, R.L. and D.L. Smith. “Analysis of response data for several organic scintillators”. *Nuclear Instruments and Methods*, 80(2):239 – 244, 1970. ISSN 0029-554X. URL <http://www.sciencedirect.com/science/article/pii/0029554X70907688>.
- [7] Heinrich and Leutz. “Scintillating fibres”. *Nuclear Instruments and Methods in Physics Research Section A: Accelerators, Spectrometers, Detectors and Associated Equipment*, 364(3):422 – 448, 1995. ISSN 0168-9002. URL <http://www.sciencedirect.com/science/article/pii/0168900295003835>.
- [8] Ivashkin, A.P., Yu.G. Kudenko, O.V. Mineev, and J. Imazato. “Scintillation ring hodoscope with WLS fiber readout”. *Nuclear Instruments and Methods in Physics Research Section A: Accelerators, Spectrometers, Detectors and Associated Equipment*, 394(3):321 – 331, 1997. ISSN 0168-9002. URL <http://www.sciencedirect.com/science/article/pii/S0168900297006578>.
- [9] Knoll, Glenn F. *Radiation Detection and Measurement*. Wiley, 2010. ISBN 9780470131480.
- [10] Koechlin, Y. and A. Raviart. *Nuclear Instruments and Methods*, 29, September 1964.
- [11] Krane, K. *Introductory Nuclear Physics*. ” John Wiley and Sons”, 1988.

- [12] Kuchmir, Franca T. and Frank J. Lynch. “Time Dependence of Scintillations and the Effect on Pulse-Shape Discrimination”. *Nuclear Science, IEEE Transactions on*, 15(3):107 –113, june 1968. ISSN 0018-9499.
- [13] Matveeva, E., Y. Panebratsev, S. Rikhvitsky, V. Stavinsky, and L. Zhiltsova. “Measurement of timing properties of the fluorescence fast component from plastic scintillators”. *Nuclear Instruments and Methods*, 179:277–281, January 1981.
- [14] Morris, C., J. Bolger, G. Hoffmann, C. Moore, L. Smith, and H. Thiessen. *Nuclear Instruments and Methods*, 137, September 1976.
- [15] Moses, W.W., S.A. Payne, W.-S. Choong, G. Hull, and B.W. Reutter. “Scintillator Non-Proportionality: Present Understanding and Future Challenges”. *Nuclear Science, IEEE Transactions on*, 55(3):1049 –1053, june 2008. ISSN 0018-9499.
- [16] Moszynski, M. and B. Bengtson. *Nuclear Instruments and Methods*, 158(0), 1979.
- [17] R. and Ruchti. “Tracking with scintillating fibers”. *Nuclear Physics B - Proceedings Supplements*, 44(13):308 – 319, 1995. ISSN 0920-5632. URL <http://www.sciencedirect.com/science/article/pii/S0920563295800492>.
- [18] Saint-Gobain Ceramics & Plastics, Inc. *Scintillation Products*, 2011.

# REPORT DOCUMENTATION PAGE

*Form Approved*  
*OMB No. 0704-0188*

The public reporting burden for this collection of information is estimated to average 1 hour per response, including the time for reviewing instructions, searching existing data sources, gathering and maintaining the data needed, and completing and reviewing the collection of information. Send comments regarding this burden estimate or any other aspect of this collection of information, including suggestions for reducing this burden to Department of Defense, Washington Headquarters Services, Directorate for Information Operations and Reports (0704-0188), 1215 Jefferson Davis Highway, Suite 1204, Arlington, VA 22202-4302. Respondents should be aware that notwithstanding any other provision of law, no person shall be subject to any penalty for failing to comply with a collection of information if it does not display a currently valid OMB control number. **PLEASE DO NOT RETURN YOUR FORM TO THE ABOVE ADDRESS.**

<b>1. REPORT DATE</b> ( <i>DD-MM-YYYY</i> ) 22-03-2012		<b>2. REPORT TYPE</b> Master's Thesis		<b>3. DATES COVERED</b> ( <i>From — To</i> ) 20 Aug 2010 - 22 Mar 2012	
<b>4. TITLE AND SUBTITLE</b>  Investigation of BCF-12 Plastic Scintillating Coherent Fiber Bundle Timing Properties				<b>5a. CONTRACT NUMBER</b>	
				<b>5b. GRANT NUMBER</b>	
				<b>5c. PROGRAM ELEMENT NUMBER</b>	
<b>6. AUTHOR(S)</b>  Gearhart, Joel S., Captain, USAF				<b>5d. PROJECT NUMBER</b>	
				<b>5e. TASK NUMBER</b>	
				<b>5f. WORK UNIT NUMBER</b>	
<b>7. PERFORMING ORGANIZATION NAME(S) AND ADDRESS(ES)</b> Air Force Institute of Technology Graduate School of Engineering and Management (AFIT/EN) 2950 Hobson Way WPAFB OH 45433-7765				<b>8. PERFORMING ORGANIZATION REPORT NUMBER</b>  AFIT/NUCL/ENP/12-M02	
<b>9. SPONSORING / MONITORING AGENCY NAME(S) AND ADDRESS(ES)</b> Mr. William Ulicny Department of Homeland Security - Domestic Nuclear Detection Office 245 Murray Dr. B410 Washington, DC 20528				<b>10. SPONSOR/MONITOR'S ACRONYM(S)</b>  DHS/DNDO	
<b>11. SPONSOR/MONITOR'S REPORT NUMBER(S)</b>					
<b>12. DISTRIBUTION / AVAILABILITY STATEMENT</b>  APPROVED FOR PUBLIC RELEASE; DISTRIBUTION UNLIMITED.					
<b>13. SUPPLEMENTARY NOTES</b>					
<b>14. ABSTRACT</b> The timing properties of BCF-12 scintillating plastic fibers arranged in a coherent bundle are investigated. An MCNP transport model is developed analyzing the interaction of neutrons with fiber bundles of varying size. A gradient in energy deposition is seen starting at the 10x10 fiber bundles onward. A 40x40 bundle has $6.7 \pm 0.2\%$ intrinsic efficiency for double scatter events. Over 40% of the double scatter events occur with a time separation of 1 ns or greater in the 40x40 bundle. The lowest dark count rate was achieved with the lens cap / aluminum can and collar system with a dark count rate of 15 per second. A bimodal distribution of scintillation pulse decay constants is discovered; these two distributions are statistically different from each other allowing real-time discrimination of dark events from scintillation events using a single PMT. A dual-ended readout technique is used to investigate scintillation pulse shapes. No significant difference is measured between the multiple peaks seen in scintillation pulses of single fibers and fiber bundles. Multiple scatter events were not detected using a 7x3 fiber bundle. Construction of a 40x40 fiber bundle is recommended for future research due to its intrinsic efficiency and measurable double-scatter event probability.					
<b>15. SUBJECT TERMS</b>  Scintillating Fibers, Neutron Detection					
<b>16. SECURITY CLASSIFICATION OF:</b>			<b>17. LIMITATION OF ABSTRACT</b>	<b>18. NUMBER OF PAGES</b>	<b>19a. NAME OF RESPONSIBLE PERSON</b>
a. REPORT	b. ABSTRACT	c. THIS PAGE			Maj Benjamin R. Kowash
U	U	U	U	100	<b>19b. TELEPHONE NUMBER</b> ( <i>include area code</i> ) (937)255-3636 x4571; benjamin.kowash@afit.edu